processes

MDPI

Article

Fluid Modeling of a Non-Thermal Plasma with Dielectric Barrier Discharge and Argon as a Diluent Gas

Cristina Mas-Peiro [1,*], Fèlix Llovell [2] and Josep O. Pou [1]

[1] Department of Chemical Engineering and Materials Science, IQS School of Engineering, Universitat Ramon Llull, Via Augusta 390, 08017 Barcelona, Spain
[2] Department of Chemical Engineering, ETSEQ, Universitat Rovira i Virgili, Avinguda Països Catalans 26, 43007 Tarragona, Spain
* Correspondence: cristinamasp@iqs.url.edu

Abstract: Non-thermal plasma (NTP) conversion applications have become an emerging technology of increasing global interest due to their particular ability to perform at atmospheric pressure and ambient temperature. This study focuses on a specific case of a dielectric barrier discharge NTP reactor for carbon dioxide conversion with the usage of argon as diluent gas. The plasma computations in COMSOL® Multiphysics are compared to experimental results and coupled with previous thermodynamic characterization of argon species and fluid dynamic calculations. The model is defined as a time-dependent study with a 2D-Geometry of pure argon, with both fluid flow and plasma phenomena. Firstly, the model showcases an accurate understanding of the plasma physics involved, in the form of electron density, excited argon, argon ions, and mean electron energy. It also allows a direct comparison of the velocity, vorticity, pressure, and dynamic viscosity results with fluid flow computations. Secondly, the impact of several variables is studied, notably the inlet volumetric rate, dielectric barrier thickness and material, and reactor length. Limitations in the plasma characterization can occur by not including packed material or all relevant species in experimental CO_2 conversion and their respective reactions, which should be aimed at in future contributions.

Keywords: non-thermal plasma; atmospheric pressure plasma; dielectric barrier discharge; plasma physics; plasma simulation; fluid flow simulation

Citation: Mas-Peiro, C.; Llovell, F.; Pou, J.O. Fluid Modeling of a Non-Thermal Plasma with Dielectric Barrier Discharge and Argon as a Diluent Gas. *Processes* **2024**, *12*, 1405. https://doi.org/10.3390/pr12071405

Academic Editors: Evgenia Benova and Frantisek Krcma

Received: 23 May 2024
Revised: 29 June 2024
Accepted: 2 July 2024
Published: 5 July 2024

1. Introduction

In recent years, cold atmospheric plasma technologies have shown great potential across wide-ranging industries, with non-thermal plasma (NTP) applications ranging from plasma jets in the biomedical field [1] to starch modification in the food industry [2] or low-temperature catalysis of products in environmental sciences [3]. The ability to produce non-thermal plasma is of particular interest in comparison with traditional thermal plasmas, as it has the advantage of being effective at atmospheric pressure and ambient temperature [4].

Non-thermal plasma can be generated in a reactor, filled with gas to be treated, by applying a potential difference between two electrodes [5–7]. This creates an electric field that accelerates electrons, causing them to collide towards molecules, thus generating ionization, excitation, and dissociation reactions. These bring about collisions in the reactor that enable reactions of different species and the dissociation of molecules in the reactor. Inside the reactor, non-thermal plasma generates very active chemical species (electrons, ground state, effective excited state, and ions), yet the energy input required can be achieved through electric power. In fact, this electrical field can even be introduced through renewable energies such as solar panels [8].

One application of non-thermal plasma of particular interest is for carbon dioxide (CO_2) conversion. Within the perimeter of carbon dioxide reduction technologies [9–12], a major limitation is the high thermodynamic stability of the CO_2 molecule, which translates into high energetic requirements to break the carbon monoxide (CO) oxygen double

bond (OC=O) and to dissociate the molecule [13]. This elevated energetic need for CO_2 dissociation ($\Delta H_{298} \sim 283.3$ kJ mol^{-1} = 2.94 eV) [14] can be tackled with cold atmospheric plasma, where electrons produced in the plasma acquire high energies between 1–10 eV [8] at ambient temperature.

Across various literature, many non-thermal plasma CO_2 reactor set-ups and configurations are investigated [15], including Gliding Arc (GA) [16], Dielectric Barrier Discharge (DBD) [17], and Microwave Plasmas [18].

A dielectric barrier discharge is understood as the electrical discharge between two electrodes covered with a layer acting as an insulator [5]. Typically, dielectric materials include quartz, ceramics, glass, enamel, mica, plastics, silicon rubber, or Teflon [19–21]. For a DBD plasma to operate, the discharge gap is usually in the range of 0.1–10 mm [22]. The variable to define the insulator capability of the material is the relative permittivity, which defines how easily a material can become polarized by imposition of an electric field. In the case of glass, the dielectric constant can range from 3.7 to 10 [23]. Other relative permittivity values of common dielectric materials can be found in later sections.

In the case of CO_2 non-thermal plasma conversion, usage of a noble gas, such as helium (He) or argon (Ar), as a diluent gas proves beneficial in the reactor's optimization [24]. This is due to the breakdown voltage of the CO_2-Ar and CO_2-He mixtures being lower than of pure CO_2. The positive effect of using an ionized noble gas is more pronounced with argon than with helium [5]. Argon is first ionized, allowing the start-up of the plasma to be initiated quicker, while CO_2 acts as a reactant since the excited argon atoms give charge and energy transfer to the more stable CO_2 molecules. Unsurprisingly, high concentrations of diluent gas are required for this effect to take place.

This study focuses on a specific case of a non-thermal DBD plasma reactor for carbon dioxide conversion with the usage of argon as diluent gas.

Great amounts of experimental work have been undertaken to study CO_2 NTP conversion reactors in a dielectric barrier. In order to secure higher CO conversion and energy efficiency results, several DBD plasma experiments have been conducted, including changing the following: applied frequency and power [25], gas flow rate [26], discharge length [27], discharge gap [26], reactor temperature [28], dielectric material [19–21], electrode material [29], diluent gases [24], and introducing catalytic packing [30].

Furthermore, extensive modeling has also been conducted to obtain a more comprehensive insight into the plasma chemistry in a DBD. Computational models of pure CO_2 conversion are possible, but only with a simplified geometrical model such as a 0D/1D-fluid [31–33]. In order to introduce laminar flow into the model, a 2D-Geometry is required, which limits the complexity of the kinetic model. A particular 2D-Geometry simulation of interest for CO_2 conversion, which combines plasma modeling with gas flow, is shown with a dual-vortex plasmatron, a variation of a GA plasma reactor [34]. Due to the added complexity of the 2D-Geometry and gas flow, this contribution includes a simplified argon plasma chemistry equivalent to the plasma chemistry proposed in this work.

Other literature of DBD non-thermal plasma simulations with pure argon is found in cold plasma jets [35–39], actuators [40], and reactors with a 1D-Geometry [41–43] or a 2D-Geometry [42,44,45]. In the case of plasma jets, contributions indicate a good agreement between experimental results and the studied physics of the plasma jets [35–39], as well as a correlation between plasma formation and gas flow rate, operating voltage, and frequency [36,39]. Literature on plasma actuators [40] has also studied the influence of electrode distance and dielectric material. Contributions on DBD reactors have shown further detail in the reaction kinetics of the argon model [42,46] or studied the effects of the applied voltage, DBD gap distance [43], and the nature of the dielectric layers [41] on reactor performance.

The aim of this work is to strengthen the correlation between the current experimental results [47] and the plasma phenomena and fluid behaviors occurring in the reactor by simulating a 2D-Geometry model with COMSOL® Multiphysics. Although extensive literature for simulations of pure argon plasmas exists, the inclusion of a computational fluid dynamic

study (CFD) in models is not as frequent. In addition, the simulation is coupled with CFD calculations of the reactor from previous contributions [48] to improve convergence, as well as thermodynamic characterization of compounds and mixtures involved [49], allowing greater precision in the plasma chemistry. Taking advantage of the controlled computation burden of these simulations, the effect of several variables is studied in hopes of improving the conversion in future reactor configurations. Finally, the correlation between fluid and plasma properties across simulations is evaluated.

2. Theory

2.1. Experimental Reactor

The dielectric barrier discharge reactor is designed as a packed-bed reactor in the laboratory setting [47]. The experimental reactor and its configuration are represented in Figure 1. It includes an inlet (left) where the mixture to be treated is introduced and an outlet (right) where the reaction products are collected.

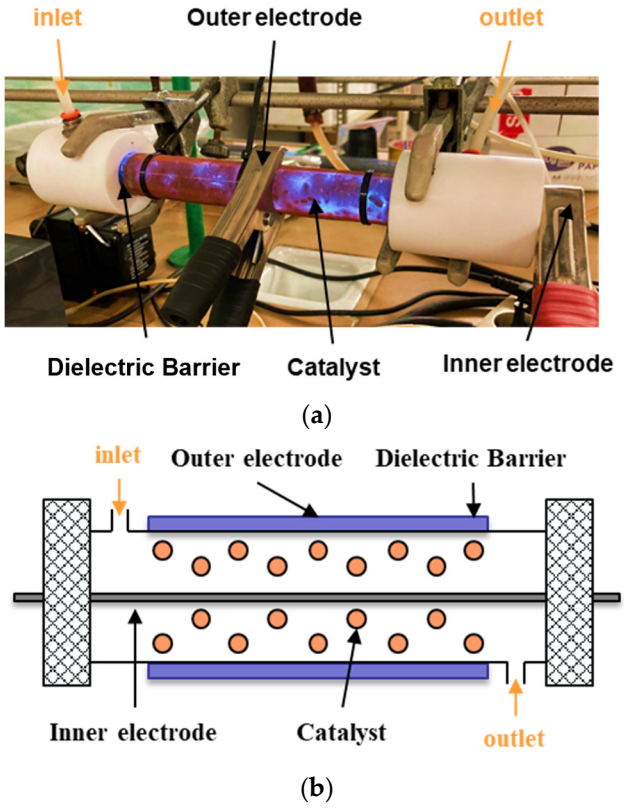

Figure 1. Non-thermal plasma reactor: (**a**) Experimental set-up and (**b**) configuration.

The configuration of the reactor defines the modeling geometry. Firstly, a cylindrical quartz tube acts as the dielectric barrier (L = 250 mm; outer diameter = 25 mm; inner diameter = 24 mm). An inner copper rod (outer diameter = 5 mm) acts as the inner electrode (anode), while the outer electrode (cathode) is a copper mesh (L = 160 mm), wrapped around the quartz cylinder. The copper mesh is held by two Teflon parts (PTFE), where gas inlet and outlet are located. The discharge gap is located within the reactor with <10 mm space.

For reference, the experimental results obtained from our previous work [47] are depicted in Table 1. To note, the minimum argon volumetric composition across all experimental cases is >95.69%. For all 36 cases, experimental yield is available.

Table 1. Experimental results (yield) with total inlet volume rate.

Study Case	Cases	Total Inlet Volume Rate (L/min)	Total Inlet Volume Rate (m^3/s)	Argon Volumetric Composition (%)	Yield (%)
1	1.1	1.045	1.74167×10^{-5}	0.9569	4.55
	1.2	1.036	1.72667×10^{-5}	0.9653	6.11
	1.3	1.030	1.71667×10^{-5}	0.9709	8.80
	1.4	1.021	1.70167×10^{-5}	0.9794	14.31
	1.5	1.015	1.69167×10^{-5}	0.9852	23.42
	1.6	1.015	1.69167×10^{-5}	0.9852	20.98
	1.7	1.009	1.68167×10^{-5}	0.9911	40.24
	1.8	1.009	1.68167×10^{-5}	0.9911	49.32
	1.9	1.006	1.67667×10^{-5}	0.9940	55.40
	1.10	1.006	1.67667×10^{-5}	0.9940	64.45
	1.11	1.003	1.67167×10^{-5}	0.9970	74.17
	1.12	1.003	1.67167×10^{-5}	0.9970	75.49
2	2.1	0.865	1.44167×10^{-5}	0.9827	13.49
	2.2	0.859	1.43167×10^{-5}	0.9895	39.00
	2.3	0.856	1.42667×10^{-5}	0.9930	51.00
	2.4	0.853	1.42167×10^{-5}	0.9965	59.10
3	3.1	0.765	1.27500×10^{-5}	0.9804	11.70
	3.2	0.759	1.26500×10^{-5}	0.9881	32.42
	3.3	0.756	1.26000×10^{-5}	0.9921	34.55
	3.4	0.753	1.25500×10^{-5}	0.9960	43.85
4	4.1	0.715	1.19167×10^{-5}	0.9790	8.37
	4.2	0.709	1.18167×10^{-5}	0.9873	27.88
	4.3	0.706	1.17667×10^{-5}	0.9915	24.04
	4.4	0.703	1.17167×10^{-5}	0.9957	35.06
5	5.1	0.665	1.10833×10^{-5}	0.9774	6.00
	5.2	0.659	1.09833×10^{-5}	0.9863	21.72
	5.3	0.656	1.09333×10^{-5}	0.9909	20.77
	5.4	0.653	1.08833×10^{-5}	0.9954	30.03
6	6.1	0.615	1.02500×10^{-5}	0.9756	4.81
	6.2	0.609	1.01500×10^{-5}	0.9852	18.25
	6.3	0.606	1.01000×10^{-5}	0.9901	18.01
	6.4	0.603	1.00500×10^{-5}	0.9950	18.91
7	7.1	0.515	8.58333×10^{-6}	0.9709	3.78
	7.2	0.509	8.48333×10^{-6}	0.9823	13.02
	7.3	0.506	8.43333×10^{-6}	0.9881	9.82
	7.4	0.503	8.38333×10^{-6}	0.9940	13.67

The calculation of the experimental yield, or CO_2 Conversion (%), was determined with the following equation:

$$CO_2\text{Conversion}(\%) = \frac{C_{CO_2,in} - C_{CO_2,out}}{C_{CO_2,in}} \times 100, \quad (1)$$

where $C_{CO_2,out}$ is the molar concentration (%) of CO_2 in the outlet stream and $C_{CO_2,in}$ is the molar concentration (%) of CO_2 in the inlet stream.

2.2. Modeling Approach

The modeling approach used in this study is represented in Figure 2. For the plasma model in the simulations, some simplifications are required.

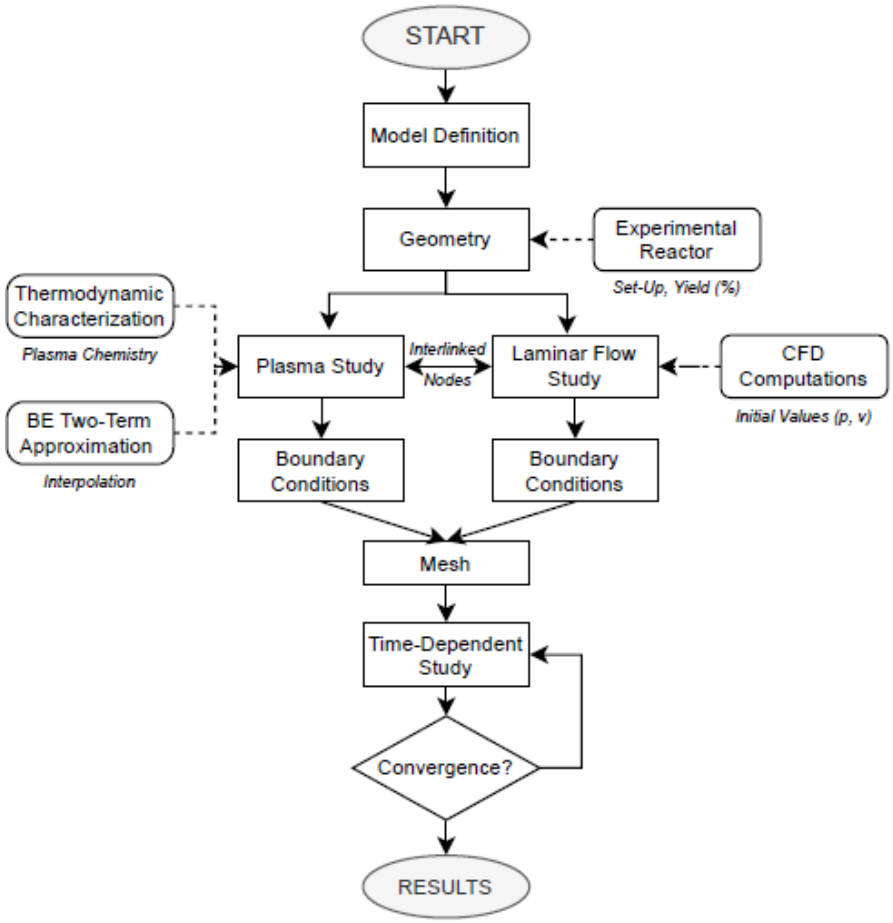

Figure 2. COMSOL® Multiphysics simulation flowchart.

Firstly, considering all chemical, thermodynamic, and fluid-dynamic interactions of the inlet and outlet mixtures would be highly intricate. This complexity cannot be tackled in a 2D-Geometry, which is required to assess the fluid flow. Considering that argon is the compound with the highest concentration (at least 95.69%) across all laboratory experiments and that it functions as a diluent gas for plasma breakdown, the characterization of the plasma is simplified by simulating argon only. Argon is the compound that not only initiates plasma (and sustains it), but also the compound that most greatly defines plasma phenomena. In addition, the chemical kinetic modeling of non-equilibrium Ar-CO_2 is only found in previous literature for thermal plasmas (Tg = 6000 K, p = 760 Torr) [50]. Other literature [34] also shows simplified plasma chemistry, most notably not accounting for the influence of vibrational states of CO_2 splitting in dielectric barrier discharges.

In order to combat this chemistry simplification, previous literature [49] is used to provide a highly accurate argon molecular model from thermodynamic characterization of the compound. This allows a more defined understanding of the molecule, as presented in Table 2. The thermodynamic behavior of argon was computed in previous work with the soft-SAFT equation [51,52], a variation of the SAFT equation of state (EoS) [53]. The Statistical Associating Fluid Theory (SAFT) equation is a molecular-based EoS developed from statistical mechanics concepts that describes thermodynamic properties of complex fluids and predicts phase equilibria. In the case of soft-SAFT, the characterization considers the Lennard–Jones (LJ) intermolecular potential for the repulsive and attractive interactions [54].

Table 2. Argon molecular model for plasma modeling.

Input Variable	Value	Reference
Molar Mass	M = 39.948 [g/mol]	[49]
Potential char. Length	σ = 3.401 [Å]	
Dispersive Energy	ε/k_B = 117.1 [K]	
Dipole Moment	μ_D = 0 [C·m]	

In summary, the soft-SAFT framework allows the description of a studied fluid with a coarse-grained model defined by the following set of molecular parameters: homonuclear chain of m spherical segments of diameter σ_{ii}, monomer–monomer dispersive energy ε/k_B, dipolar (μ) or quadrupolar (Q) moment, and fraction of segments containing the polar moment (x_p). In the case of argon, as an apolar spherical molecule, the chain length can be set at m = 1 and the dipole moment at μ_D = 0 Debye.

This set of molecular parameters is sufficient to characterize argon, which was obtained by fitting to experimental equilibrium data (liquid density and vapor pressure data) in previous contributions [49]. The molecular model of argon can be introduced in the simulation tool directly when defining each species (ground state Ar, excited state Ar*, and argon ion Ar^+).

Secondly, in order to introduce fluid flow and study the effect of inlet volumetric rate, a 2D-Geometry is required. This implies that the axisymmetric geometry must be provided with some simplification. The location of the inlet and outlet cannot be placed left and right, respectively; therefore, the boundary conditions are introduced at the bottom and top walls. This assumption creates some discrepancies regarding plasma discharge behavior, where the simulation forms sheaths against the walls while the experimental plasma may initiate at the inlet and outlet locations. In fact, the fluid flow within the PTFE parts themselves is not assessed, as is the case with previous literature [48], but the laminar flow is simulated inside the plasma domain, where reactions occur. The range of total inlet volumetric rate in the inlet is taken from experimental data: 0.503–1.045 L/min.

All input variables to define the plasma are included in Table 3.

Table 3. Input variables for plasma modeling.

Input Variable	Value	Reference
Voltage (maximum)	1 kV	[47]
Frequency (minimum)	20 kHz	[47]
Plasma Temperature (oven)	60 °C	[47]
Reactor Length	160 mm	[47]
Total Inlet Volumetric Rate	0.503–1.045 L/min	[47]
Relative Permittivity Quartz	ε_r = 4.2	[55]

In addition, although the total DBD length is 250 mm, the copper mesh only covers a length of 160 mm. The shorter length is the actual length for which the plasma domain must be simulated. In the model, the mesh is simplified to a thin copper foil. No further specification is required for the mesh since experimentally the discharge reported at the given conditions is homogeneous. Previous contributions [56] also showcase homogeneous discharge of argon with the introduction of fine mesh electrodes.

Lastly, the remaining elements also presented in the table to define the model are the experimental (voltage, frequency, and plasma temperature) values as well as the relative permittivity of the dielectric barrier.

2.3. Modeling Geometry

The modeling studies in this work are performed using the commercial software package COMSOL® Multiphysics Version 6.1, for which a modeling geometry must be defined.

Previous contributions [57] have tackled a simplified 1D-Geometry model of the reactor, which serves as a basis for this work. The 1D-Geometry study demonstrates the argon breakdown, initiation of the plasma after the first RF cycle, generation of electrons, and effect of secondary emissions and dielectric barrier at the given reactor conditions.

A simple 1D-Geometry shows a quick way to gain insight into the characteristics of the argon plasma discharge without excessive computational burden. However, the 1D-Model is limited as it cannot account for the fluid's movement. To couple the plasma phenomena with a computational fluid dynamics study, a 2D-Model is required.

In principle, the known reactor should be studied as a 3D-Geometry to consider the entirety of the catalyst packaging and the laminar flow of the mixture. However, the duration of such 3D simulations with the entirety of reactions is estimated to exceed weeks or months with current technology. Due to these computational limitations, a 2D-Geometry of pure argon is proposed in this work with a time-dependent study. The representation of the 2D-Geometry is depicted in Figure 3, which rotates around the Z-axis to a cylindrical shape.

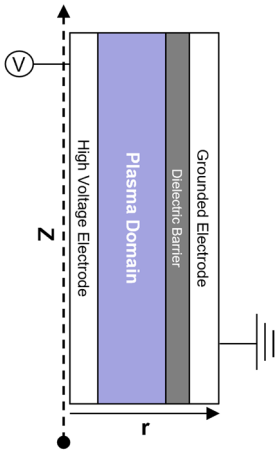

Figure 3. Non-thermal plasma configuration in a 2D-Geometry (axisymmetric).

The mesh introduced in the model is visualized (for Z < 40 mm) in Figure 4.

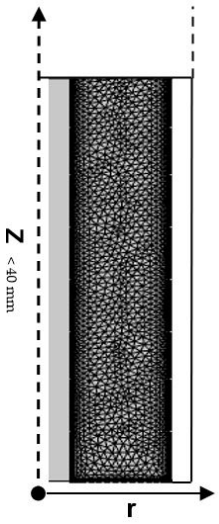

Figure 4. Mesh size visualization in a 2D-Geometry (axisymmetric).

The mesh definition strongly determines the calculation effort of the model, as well as its accuracy. In most areas, a mesh size between fine and normal can be introduced, while a finer mesh is inserted in the boundary walls. The length of the reactor limits the finesse of the mesh due to the computational effort incurred. To quicken computations, initial values of velocity and pressure are introduced as per previous CFD contributions [48].

Once the 2D-Geometry is defined, the effect of several variables can be studied to allow an understanding of the optimization of plasma. While every simulation in the sensitivity study can differ in computational time or geometry, the mesh element size is kept constant across all computations.

3. Model

3.1. Governing Equations

The model is completed with the built-in Plasma Module and Laminar Flow Modules in COMSOL® Multiphysics, which not only considers the governing equations and boundary conditions for the fluid model and plasma model separately but also inherently studies the multiphysics interactions between the two. All governing equations are expressed as follows and extracted from the CFD Module and Plasma Module User Guides, respectively [58,59].

3.1.1. Fluid Model

The computational flow dynamics study is possible through the inclusion of the gas flow through the Laminar Flow Module in the 2D-Model. As with other CFD studies, the Navier–Stokes equations for mass and momentum conservation are solved. These describe how the velocity, pressure, and density of a moving fluid are related. The governing equations for fluid regions are presented in the following equations below:

$$\nabla \times [-p\mathbf{I} + \tau] + \boldsymbol{F} = \rho \frac{\partial \boldsymbol{u}}{\partial t} + \rho(\boldsymbol{u} \times \nabla)\boldsymbol{u} \tag{2}$$

$$\frac{\partial \rho}{\partial t} + \nabla \times (\rho \boldsymbol{u}) = 0, \tag{3}$$

where p is the pressure, τ the viscous stress tensor, $\boldsymbol{F}$ the fluid body force vector, ρ the density of the mixture, and $\boldsymbol{u}$ the mass averaged fluid (or gas flow) velocity vector.

In conjunction with the CFD equations, boundary conditions (BC) must also be specified. For the fluid-dynamic study, the BCs are expressed in the inlet (volumetric flow rate) as well as in the outlet (ambient pressure). The ranges of the volumetric inlet rates are specified in Table 3. The full view of model's boundary conditions is presented at the end of this section.

The assumption of the classic governing equation previously presented is of laminar, fully developed flow. In the presented geometry model, only laminar flow occurs since the Reynolds number (R_E) does not reach levels of turbulent flow. The characterizing length is the inlet diameter L = 5 mm of the reactor, while the total flow rate ranging from 0.503 to 1.045 L/min determines the v velocity of the flow. In the case of pure argon, at room temperature and atmospheric pressure, the fluid density equals to ρ = 1.641 kg/m^3 and the absolute viscosity of the fluid equals to $\mu = 2.23 \times 10^{-5}$ Pa·s. This would equate to R_E ranging from 13.643 to 28.445. For reference, even at the highest reaching velocities within the reactor (max: 0.0859 m/s), the flow would remain laminar, as it only starts becoming intermittent at around 6.3 m/s velocity flow. Thus, the flow within the reactor in all cases is laminar.

3.1.2. Plasma Model

Using the built-in Plasma Module in COMSOL® Multiphysics, the plasma model is solved with a set of coupled differential equations that express the conservation of mass, momentum, and energy for the different plasma species. These are noted as various governing equations, i.e., drift-diffusion, heavy species transport, rate of reaction for plasma chemistry and Poisson's equation for the electrostatic field.

The electron density and mean electron energy are computed by solving a pair of drift-diffusion equations as follows:

$$\frac{\partial}{\partial t}(n_e) + \nabla \times [-n_e(\mu_e \times \boldsymbol{E}) - \boldsymbol{D}_e \times \nabla n_e] = R_e \tag{4}$$

$$\frac{\partial}{\partial t}(n_\varepsilon) + \nabla \times [-n_\varepsilon(\mu_\varepsilon \times \boldsymbol{E}) - \boldsymbol{D}_\varepsilon \times \nabla n_\varepsilon] + \boldsymbol{E} \times \Gamma_e = R_\varepsilon, \tag{5}$$

where $\boldsymbol{E}$ is the electric field, R_e the electron source, R_ε the energy loss due to inelastic collisions, μ_e the electron mobility, μ_ε the energy mobility, n_e the electron density, n_ε the electron energy density, and Γ_e the electron flux.

The diffusivity and mobility elements are computed as per the following equations:

$$\boldsymbol{D}_e = {}_eT_e, \ {}_\varepsilon = \left(\frac{5}{3}\right)_e, \ \boldsymbol{D}_\varepsilon = {}_\varepsilon T_e \tag{6}$$

The electron temperature is defined as follows:

$$T_e \ = \left(\frac{2}{3}\right)\bar{\varepsilon}, \tag{7}$$

where $\bar{\varepsilon}$ is the mean electron energy computed as the division between the electron energy density (n_e) and the electron energy density (n_ε).

In addition, the source coefficients are determined by using rate coefficients. Firstly, the electron source term is given by the following:

$$R_e = \sum_{j=1}^{M} x_j k_j N_n n_e, \tag{8}$$

where x_j is the mole fraction of the target species for reaction j, k_j the rate coefficient for reaction j, and N_n the total neutral number density.

Secondly, the electron energy loss is the sum of the collisional energy loss over all reactions.

$$R_\varepsilon = \sum_{j=1}^{P} x_j k_j N_n n_e \Delta\varepsilon_j, \tag{9}$$

where $\Delta\varepsilon_j$ is the energy loss from reaction j. The rate coefficients are computed by cross-section data, following the integral:

$$k_k = \gamma \int_0^\infty \varepsilon \, \sigma_k(\varepsilon) f(\varepsilon) d\varepsilon, \tag{10}$$

where $\gamma = \left(\frac{2q}{m}\right)^{1/2}$, m is the electron mass, q the unit charge, ε the electron energy, σ_k the collision cross section, and f the electron energy distribution function (EEDF).

In this work, plasma behavior has been modeled as a non-Maxwellian fluid, which can be computed with an approximation of the Boltzmann equation (BE). The Boltzmann equation expresses the evolution of the distribution function, f, in a six-dimensional phase space as follows:

$$\frac{\partial f}{\partial t} + \boldsymbol{v} \times \nabla f - \frac{e}{m}(\boldsymbol{E} \times \nabla_v f) = C[f], \tag{11}$$

where $\boldsymbol{v}$ is the velocity coordinates, e is the elementary charge, ∇_v the velocity-gradient operators, and C represents the rate of change in f due to collisions.

A common approach to simplifying the BE is the so-called two-term approximation. When the Boltzmann equation, two-term approximation (linear) is selected in COMSOL®, the EEDF is computed from a partial differential equation instead of taking an assumed function. Further details on the approach are described in the Plasma Chemistry section.

For non-electron species, the mass fraction of each species is solved with the heavy species transport equation, as follows:

$$\rho \frac{\partial}{\partial t}(w_k) + \rho(\boldsymbol{u} \times \nabla)\, w_k = \nabla \times \boldsymbol{j}_k + R_k, \tag{12}$$

where w_k is the mass fraction for species k, $\boldsymbol{j}_k$ is the diffusive flux vector for species k, and R_k is the rate expression for species k.

Finally, the Poisson equation is solved for the electric field distribution, using the densities of the different charged plasma species as input in the discharge gap and solving for zero space charge in the dielectric material.

$$\nabla \times (\varepsilon_0 \varepsilon_r \boldsymbol{E}) = -\nabla \times (\varepsilon_0 \varepsilon_r \nabla V) = \rho_v, \tag{13}$$

where ε_0 is the permittivity of vacuum, ε_r the relative permittivity of the material or the gas, V is the potential, and ρ_v is the space charge density.

The space charge density ρ_v is automatically computed based on the plasma chemistry introduced in the model.

To complete the model, several boundary conditions must be set. The boundary condition for the electric potential on the two electrodes is imposed, considering 0 V for the grounded electrode and $V(t)$ for the powered electrode.

The discharge is driven by a sinusoidal electric potential applied to the anode, as follows:

$$V(t) = -V_0 \sin(\omega t), \tag{14}$$

where V_0 is the applied peak voltage and ω is the angular frequency.

The dielectric geometry is treated with an insultation boundary condition, setting the normal fluxes of electrons and electron energy on the boundary to zero, as well as a zero-charge boundary condition that defines the normal electric displacement equal to zero.

The governing equation for surface charge accumulation is as follows:

$$-\boldsymbol{n} \times \boldsymbol{D} = \rho_s, \tag{15}$$

where $\boldsymbol{D}$ is the electric displacement and ρ_s is the surface charge density, solved by the distributed ODE as follows:

$$\frac{d\rho_s}{dt} = \boldsymbol{n} \times \boldsymbol{J}_i + \boldsymbol{n} \times \boldsymbol{J}_e, \tag{16}$$

where $\boldsymbol{n} \times \boldsymbol{J}_i$ is the normal component of the total ion current density at the wall, and $\boldsymbol{n} \times \boldsymbol{J}_e$ is the normal component of the total electron current density at the wall.

In addition, the electron motion is defined by the boundary conditions for the electron flux and the electron energy flux, provided below.

$$\boldsymbol{n} \times \Gamma_e = \left(\frac{1}{2} \nu_{e,th} n_\mathrm{e}\right) - \sum_p \gamma_p (\Gamma_p \times \boldsymbol{n}) \tag{17}$$

$$\boldsymbol{n} \times \Gamma_\varepsilon = \left(\frac{5}{6} \nu_{e,th} n_\mathrm{e}\right) - \sum_p \varepsilon_p \gamma_p (\Gamma_p \times \boldsymbol{n}), \tag{18}$$

where γ_p is the secondary emission coefficient, ε_p is the mean energy of the secondary electrons, Γ_e is the electron flux, Γ_ε is the electron energy flux, Γ_p is the ion flux of the p-th positive ion species at the wall, and $\nu_{e,th}$ is the thermal velocity. Further information on the secondary electron emission (SEE) coefficient and mean energy is found in the Plasma Chemistry section.

In the case of heavy species, the ions are lost to the wall due to surface reactions and considering that the electric field is directed toward the wall.

$$\boldsymbol{n} \times \boldsymbol{j}_k = M_w R_k + M_w c_k Z \mu_k (\boldsymbol{E} \times \boldsymbol{n})\ [Z_k \mu_k (\boldsymbol{E} \times \boldsymbol{n}) > 0], \tag{19}$$

where M_w is the molecular weight for species k, c_k is the molar concentration for species k, Z_k is the charge number for species k, and μ_k is the mixture averaged mobility for species k.

The full detail of the model's BC is provided in Table 4.

Table 4. Boundary conditions for fluid and plasma models.

Model	Location	Description
Fluid	Inlet	Volumetric Flow Rate
	Outlet	Ambient Pressure
Plasma	Wall (Anode)	Powered Electrode $V(t)$
	Wall (Cathode)	Grounded Electrode 0 V
	Wall (all)	Electron Flux
	Wall (all)	Electron Energy Flux
	Wall (Anode and Cathode)	Surface Reactions
	Wall (Dielectric)	Surface Charge Accumulation

3.2. Plasma Chemistry

In effect, the main elements of plasma chemistry are its species and properties, including transport coefficients, electron impact reactions, heavy species reactions, and surface reactions. The overall reaction kinetics model of argon includes the same species and reaction kinetic processes as earlier works [34,39,41] for 2D-Geometries, shown in Table 5. The collision cross-sections and electron energy for the elastic and ionization reactions presented are taken from existing literature [60,61] as some previous contributions.

Table 5. Plasma reactions of argon and its species.

Reaction	Formula	Type	ΔE (eV)	Rate (m^2/s·mol)
R1	e + Ar ⇒ e + Ar	Elastic	m_R = 0.0000136	-
R2	e + Ar ⇒ e + Ar*	Excitation	11.5	-
R3	e + Ar* ⇒ e + Ar	Superelastic	−11.5	-
R4	e + Ar ⇒ 2e + Ar^+	Ionization	15.8	-
R5	e + Ar* ⇒ 2e + Ar^+	Ionization	4.427	-
R6	Ar* + Ar* ⇒ e + Ar + Ar^+	Penning ionization	-	3.3734×10^8
R7	Ar* + Ar ⇒ Ar + Ar	Metastable quenching	-	1807

Briefly, the model comprises the chemistry of four species, i.e., electrons, ground state, an effective excited state, and an ion. The five electron impact reactions can be categorized as either elastic, excitation, ionization, or attachment. Heavy species reactions such as penning ionization and metastable quenching reactions are also incorporated in the model.

The surface reactions are also specified, which automatically sets a flux boundary condition for heavy species that is proportional to the species' velocity. In this model, the ions that reach the wall are assumed to change back to neutral argon atoms and donate their charge to the wall.

Secondary emission parameters are also included for each wall boundary. The secondary emission coefficients are provided from previous contributions, while the mean energy of secondary electrons can be computed as the value for the ionization energy of the reactant (15.8 V for argon ions) minus twice the work function of the surface, the latter available from experimental literature. References and further details of the SEE coefficients and mean energy are provided in the table below in Table 6.

Table 6. Secondary emissions coefficients (γ_p) and mean energy of secondary electrons (ε_p).

Location	γ_p	Ref.	ε_p	Ref.
Wall (left)	0.08	[62]	6.580	[63]
Wall (right)	0.2	[64]	6.154	[65]

The behavior of the non-thermal plasma is non-Maxwellian, which can be computed with the two-term approximation of the Boltzmann equation. This consideration is visualized in the flowchart, Figure 2, from earlier sections. The COMSOL® tool allows the series to be truncated after the second term with the so-called two-term approximation. As introducing the BE two-term approximation in a 2D-Model would imply excessive computational efforts, the following three-step procedure is advised: firstly, create a global model in 0D with the Boltzmann equation, two-term approximation interface; secondly, export the data from the interface using a parametric extrusion dataset; and thirdly, import the data to the 2D-Model with an interpolation EEDF function.

4. Results and Discussion

4.1. Example Case Analysis

The results of this time-dependent study across various time iterations are presented below. The graphics are focused on a zoom-in (approx. length < 40 mm) for visualization purposes but are representative of the full-length reactor's behavior. A planar view is provided in the graphs, noting the axisymmetric 2D-Geometry rotates around the *Z*-axis to a cylindrical shape as per Figure 3.

The results below are initially given for a specific example case (Case 1.5 in Table 1). All results are presented at the same time incidents (t_1 = 0.57225 µs, t_2 = 2.432 µs, t_3 = 12.446 µs, t_4 = 31.187 µs, t_5 = 50.072 µs, and t_6 = 74.535 µs) and applied voltage ($V(t_1)$ = −658.72 V, $V(t_2)$ = −85.35 V, $V(t_3)$ = −999.98, $V(t_4)$ = 701.49 V, $V(t_5)$ = −9.05 V, and $V(t_6)$ = −58.40 V), respectively, following equation (15)). For this case, the fluid flow model boundary conditions are determined with an inlet volume rate of 1.015 L/min = 1.69167 × 10^{-5} m^3/s and atmospheric pressure in the outlet.

4.1.1. Electron Density

The evolution of electron density for the example case reactor is presented in Figure 5 across various time iterations. At first-time iterations, the initial spark of the plasma occurs when the electric field is generated. This electric field causes so-called gas breakdown, where the argon gas breaks up into positive ions and electrons. The early time iterations as indicated in Figure 5a show the initiation of plasma breakdown resulting in free electrons in movement. The plasma evolves until reaching a stead state starting at 12.446 µs, as seen in Figure 5c.

In later iteration times, the electric field causes the acceleration of the electrons, which collide towards gas molecules, resulting in ionization, excitation, and dissociation reactions. It is only then that excited argons start to appear, as can be seen in Figure 6. Along iteration times, not only does the position of the electrons change, but also the magnitude of the electron density. The plasma then continues to evolve, creating a plasma sheath at the walls and changing in electron density magnitude even after the first cycle (at 50 µs) as per Figure 5e.

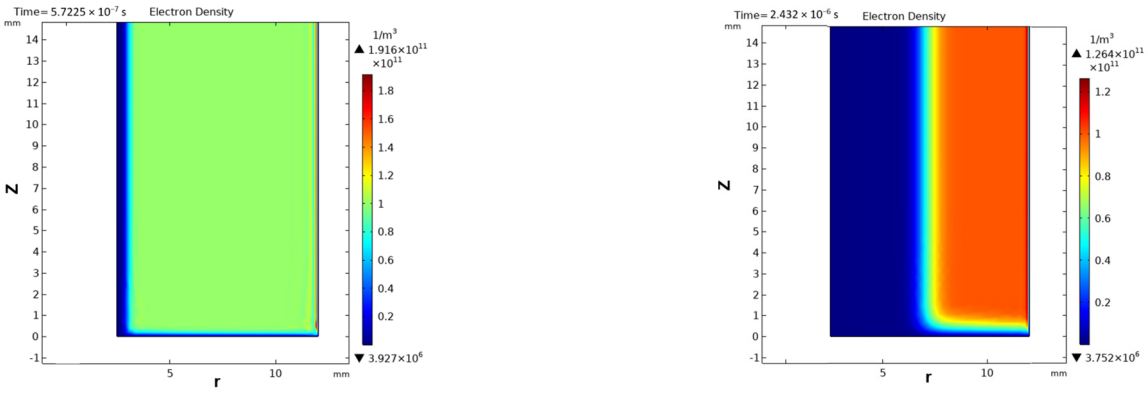

(**a**) (**b**)

Figure 5. *Cont.*

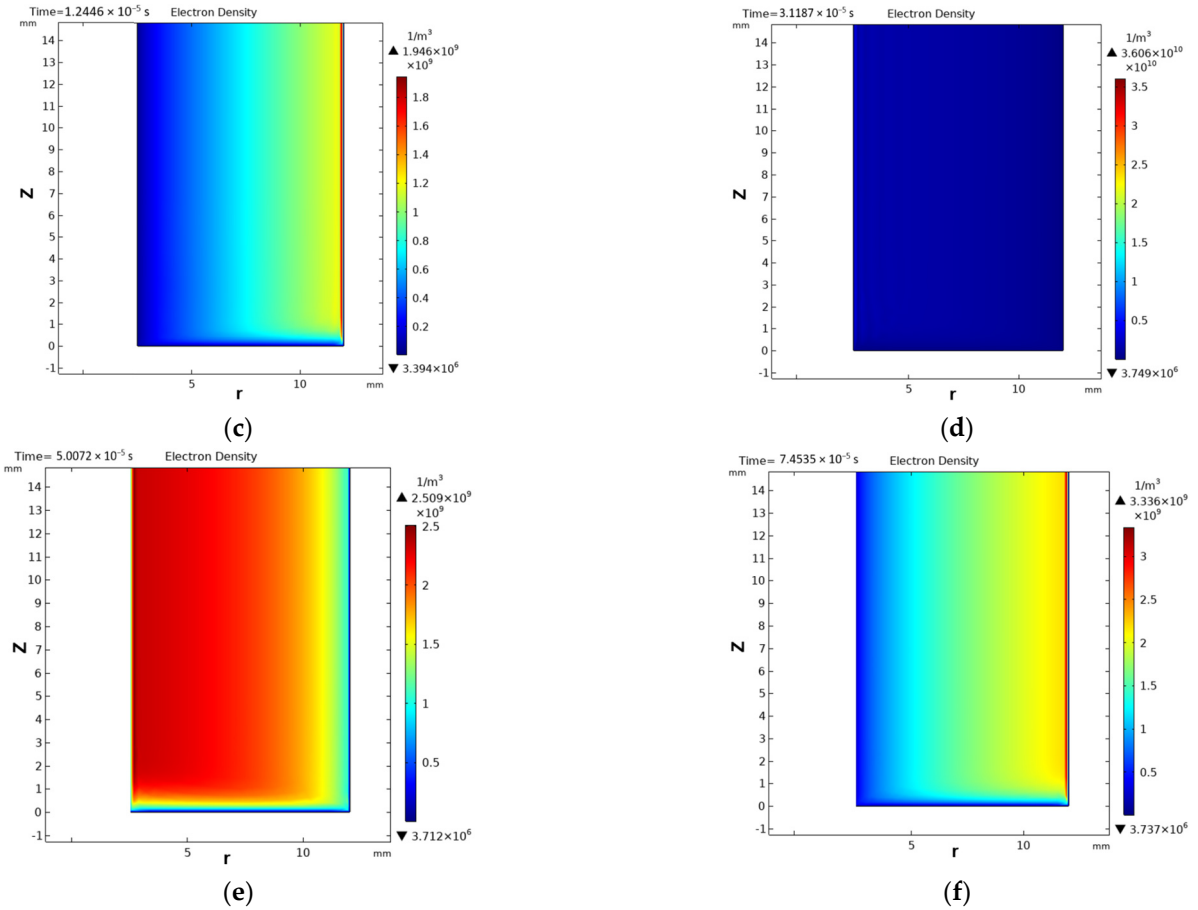

Figure 5. Electron density ($1/m^3$) for an experimental reactor across time incidents: (**a**) 0.57225 µs, (**b**) 2.432 µs, (**c**) 12.446 µs, (**d**) 31.187 µs, (**e**) 50.072 µs, and (**f**) 74.535 µs.

As seen in Figure 7, the positive ions generated are also accelerated by the electric field towards the walls, where secondary emissions occur. The secondary emissions also bring further electrons, as seen from Figure 5c onwards, making the plasma self-sustaining.

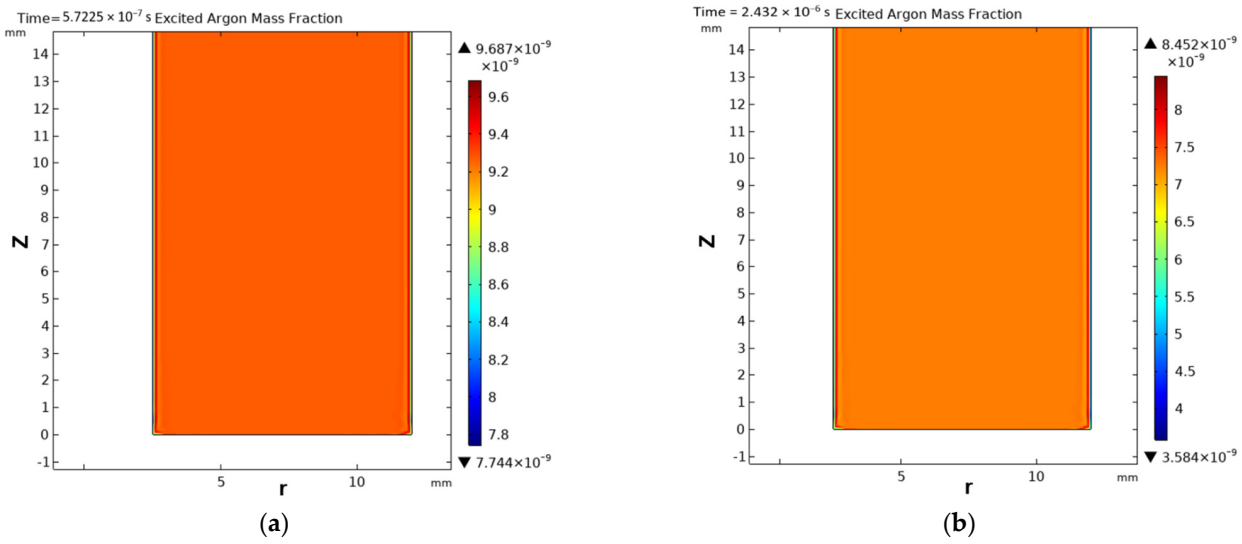

Figure 6. *Cont.*

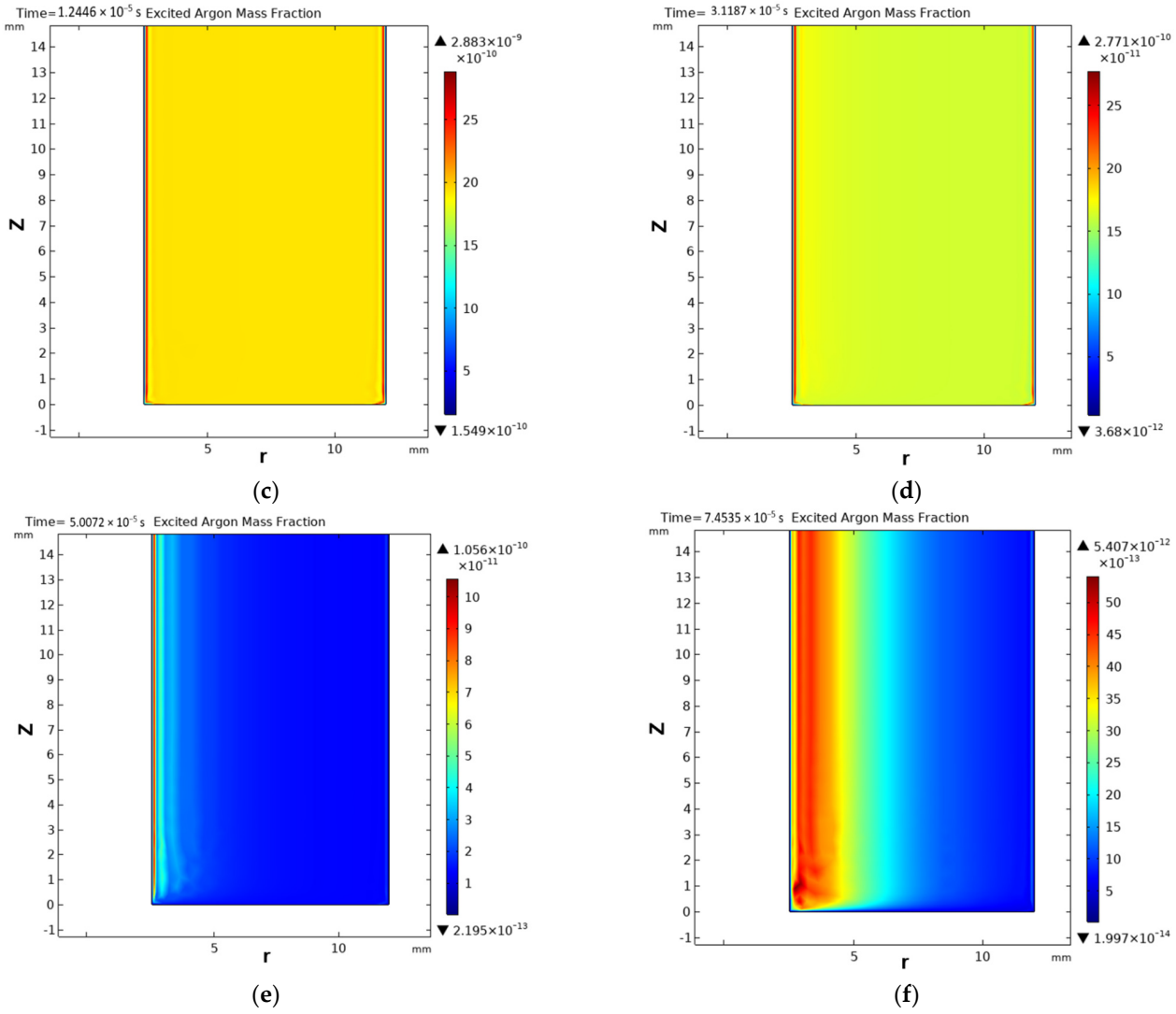

Figure 6. Excited argon mass fraction for an experimental reactor across time incidents: (**a**) 0.57225 µs, (**b**) 2.432 µs, (**c**) 12.446 µs, (**d**) 31.187 µs, (**e**) 50.072 µs, and (**f**) 74.535 µs.

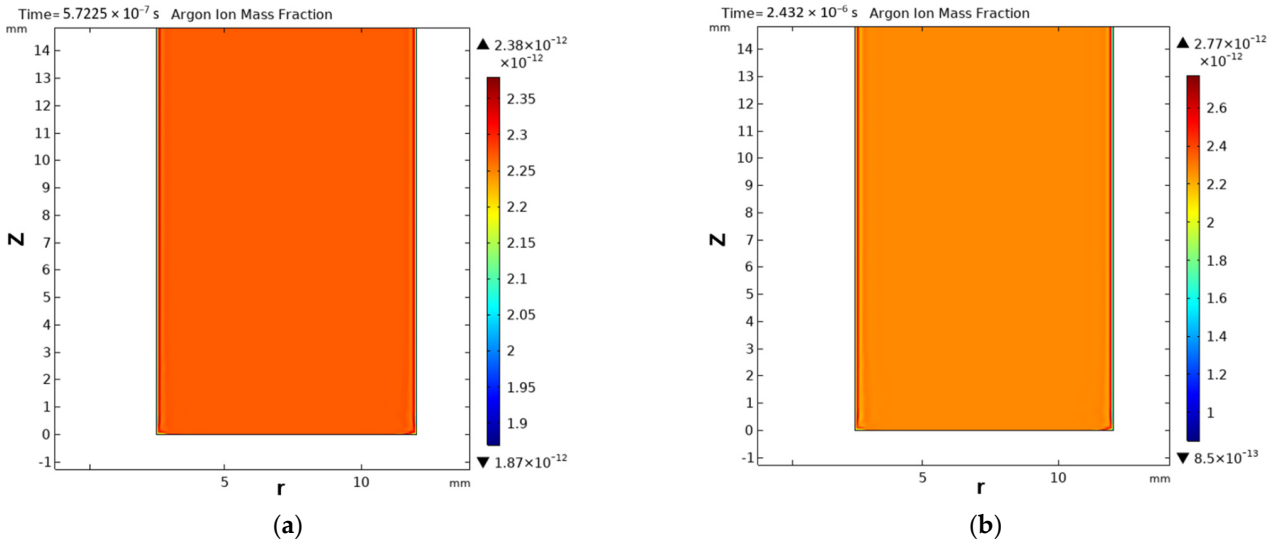

Figure 7. *Cont.*

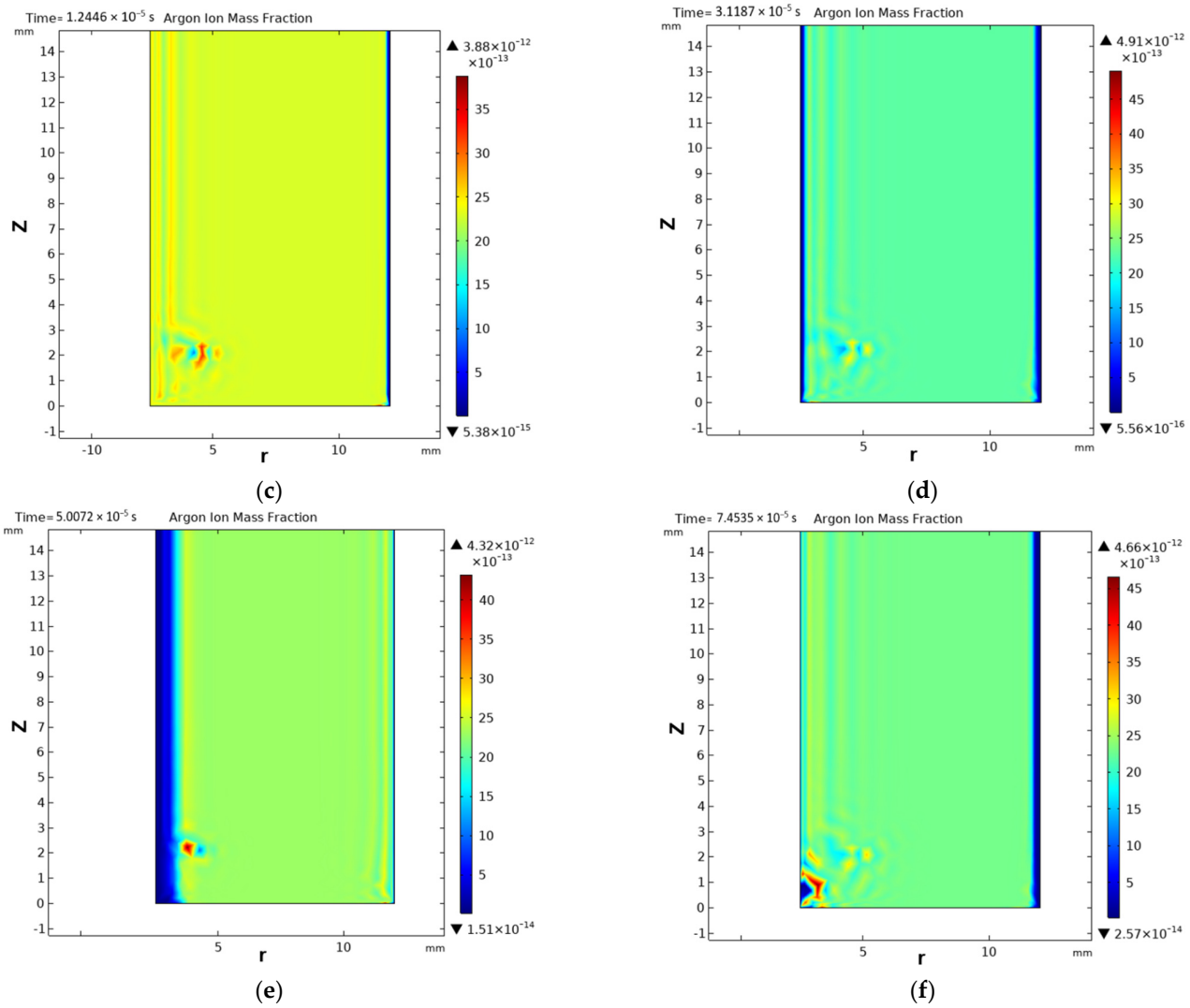

Figure 7. Argon ion mass fraction for an experimental reactor across time incidents: (**a**) 0.57225 µs, (**b**) 2.432 µs, (**c**) 12.446 µs, (**d**) 31.187 µs, (**e**) 50.072 µs, and (**f**) 74.535 µs.

When comparing Figures 5 and 6, it can be noted that the electrons act in a mirrored manner with the generation of the plasma; the electron density drops as soon as the excited argon atoms are generated. Nonetheless, the movement of the electrons versus that of the excited argon atoms is not fully symmetrical. This is due to the fact that excited argon atoms can only reach the wall via diffusion, whereas the electrons and ions reach the wall very rapidly due to migration. Thus, the movement of electrons reflects more directly the behavior of the electric field rather than that of the excited species.

4.1.2. Mass Fraction of Excited Argon Atoms and Argon Ions

The evolution of the excited argon and the argon ions throughout plasma formation across time incidents is seen on Figures 6 and 7, respectively.

Inside the discharge gap, both excited argons and argon ions are found. As previously mentioned, the behavior between the two is not fully equivalent since the movement of the relevant species (electrons, ions, ground state, metastable atoms) is not analogous due to their nature, in addition to the effect of the secondary emissions of electrons at certain walls.

Once the plasma reaches a steady state, it is interesting to focus near the walls where the highest concentrations are found. After the first cycle, as per Figure 6e, the highest concentrations are maintained near the anode but also near the dielectric barrier. The dielectric property of the material allows the barrier to act as an insulator, not allowing

current to pass through. Its dielectric constant and thickness, in combination with the time derivative of the applied voltage, dU/dt, determine the amount of displacement current that can be passed through the dielectric. This insulator effect can also be observed in Figure 6, where a buffer is formed next to the dielectric cover. In fact, the electric field in the dielectric materials should be much stronger than in the gap, which is due to the surface charge accumulating on the dielectric surfaces and tends to shield out the electric field.

It is significant to note that the experimental conversion reactor in question is for carbon dioxide and utilizes argon as the ionized gas at high concentrations. As previously stated, this is beneficial since the breakdown voltage required for the CO_2-Ar mixture is lower than that of pure CO_2. As only argon is simulated here, to understand the conversion to CO, the focus must be on the collisions of all species in the reactor. These collisions create radicals that provide enough energy to break the OC=O bond and form new compounds. It is expected that the higher the electron density of excited argon atoms and argon ions, the higher the probability of collisions to occur, and the more the collisions occur, the higher the probability of CO to be generated. Thus, although the CO_2 molar composition is not quantifiable with the simulation, the probability of CO to be generated can be linked to the electrons, ions, and excited atoms produced.

4.1.3. Mean Electron Energy

The behavior of the mean electron energy is represented in Figure 8.

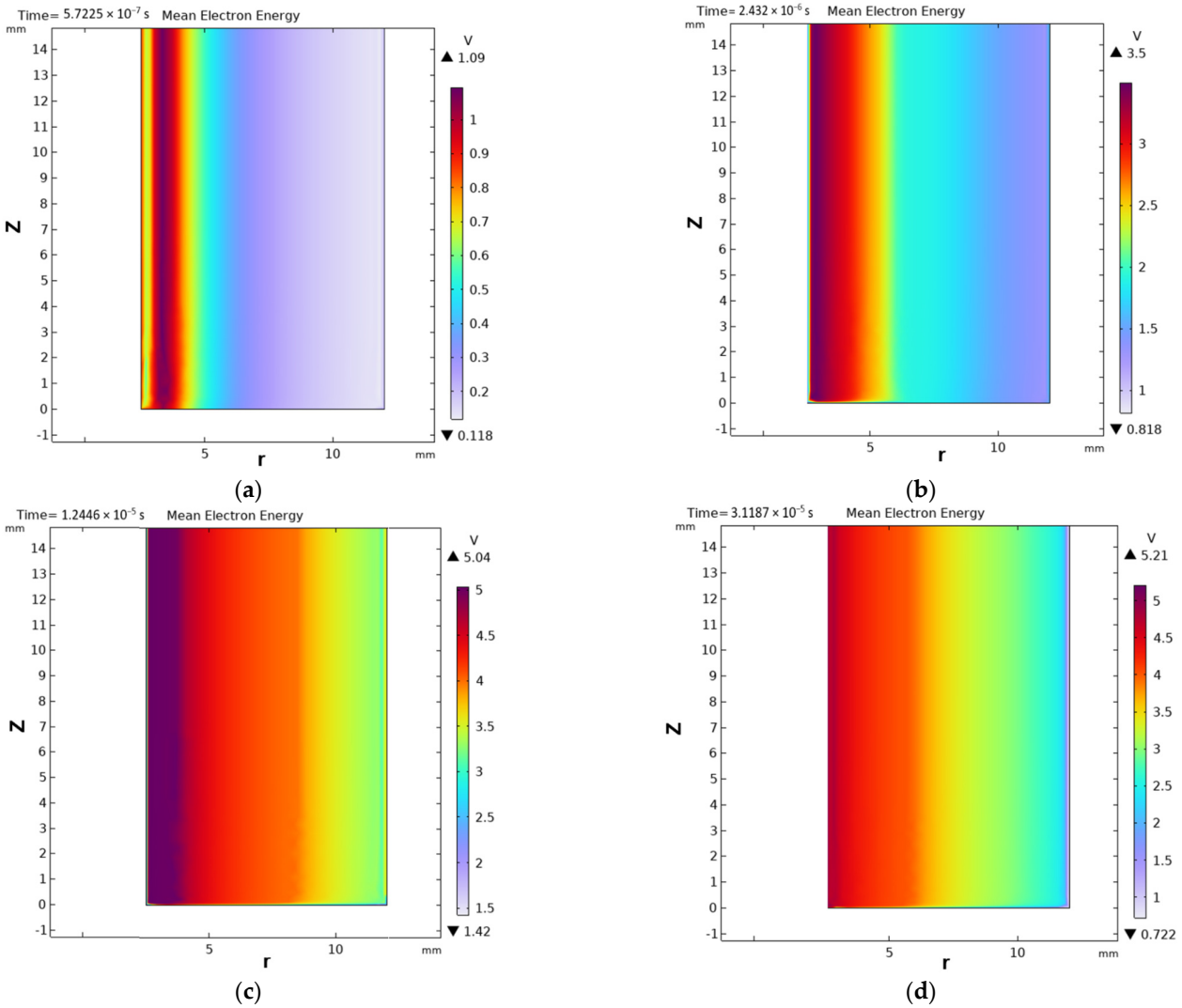

Figure 8. *Cont.*

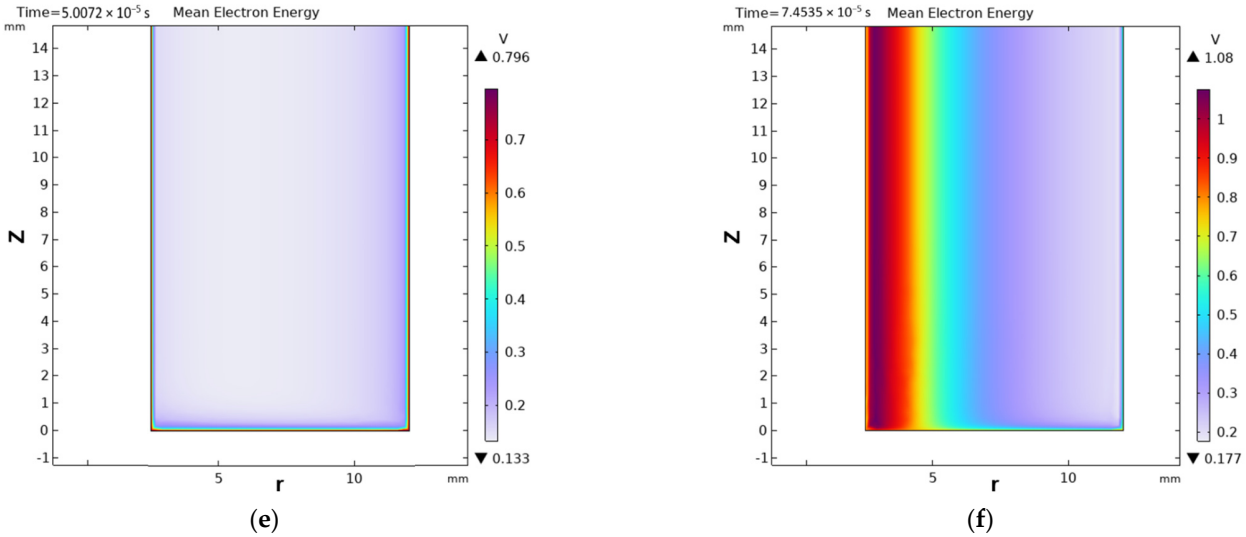

Figure 8. Mean electron energy for an experimental reactor across time incidents: (**a**) 0.57225 µs, (**b**) 2.432 µs, (**c**) 12.446 µs, (**d**) 31.187 µs, (**e**) 50.072 µs, and (**f**) 74.535 µs.

Firstly, electron energy is always concentrated at the left of the geometry, thus near the terminal generating the electric field. Across iteration times, from Figure 8a–d, it fades out evenly along the radius of the reactor.

Secondly, it can be noted that the magnitude of the energy increases from initial plasma generation until reaching its stabilization. Once excited argon atoms start being generated, the magnitude of the mean energy in the reactor increases, up to Figure 8d with a maximum of 5.21 V. The mean energy subsequently decreases analogously to the plasma behavior. As expected, when reaching the first cycle of electric potential, Figure 8e, the reactor reaches its minimum energy. The mean energy electron energy only starts to increase again at later time iterations, as per Figure 8f at 74.535 µs.

The graphs indicate that the mean electron energy should be sufficient to break the OC=O double bound, as referenced in the introduction (∼2.94 eV). This magnitude is achieved once the plasma reaches a steady state starting at 12.446 µs and is obtained at various time iterations along the electric potential cycle.

To note, the characterization of the electron temperature shows a proportional behavior to the mean electron energy.

4.1.4. Velocity, Vorticity, Pressure, and Dynamic Viscosity

In the following section, the results of the laminar flow model are reviewed. While the plasma results have been noted until now, the computational fluid dynamic result can also be studied, namely the velocity (m/s), vorticity (1/s), pressure (Pa), and dynamic viscosity (mPa·s) at a specific time incident (t = 12.446 µs).

As seen in Figure 9a, the behavior of the fluid velocity is represented in a 3D surface plot. The highest velocity is found at the inlet and outlet ends, reaching a maximum of v = 0.0367 m/s. This high velocity is maintained in the vicinity of all walls, decreasing towards the inner copper rod, where a velocity of around v = 0.02067 m/s is maintained. The fluid flow travels homogeneously across the reactor, where plasma phenomena occur. To note, too high a velocity may not allow enough time for efficient plasma reactions, but a velocity that is too slow might limit the required inflow of diluent gas.

Another variable of interest is the vorticity, representing the rotational motion of the fluid in the reactor, depicted in Figure 9b in a 3D representation plot. The rotational motion is highest in the vicinity of the walls, most significantly near the dielectric barrier, reaching a maximum of 41.0993 1/s. The average vorticity across time iterations remains at approximately 9.3821 1/s inside the reactor. By contrast, the vorticity remains low in the discharge gap, allowing an adequate fluid mixture where most plasma phenomena occur.

An excessively high rotational motion in the discharge gap could enable fluid mixing but might impede efficient plasma reactions, thereby affecting the reactor's conversion rate.

Similarly, the pressure is assessed in Figure 9c. As with non-thermal plasmas, the reactor operates at atmospheric pressure. In the simulation, the pressure is maintained, as expected, at around 101,325 Pa across time iterations. There is a minor drop in pressure alongside the reactor, which is negligible.

Lastly, the dynamic viscosity is represented in Figure 9d. The value of the dynamic viscosity varies very minimally within the reactor, having an average value of 25.245 mPa·s. The highest dynamic viscosity is seen at the edge of the walls, where the electrons are emitted, while the lowest dynamic viscosity occurs in the center of the reactor, where the reactions occur.

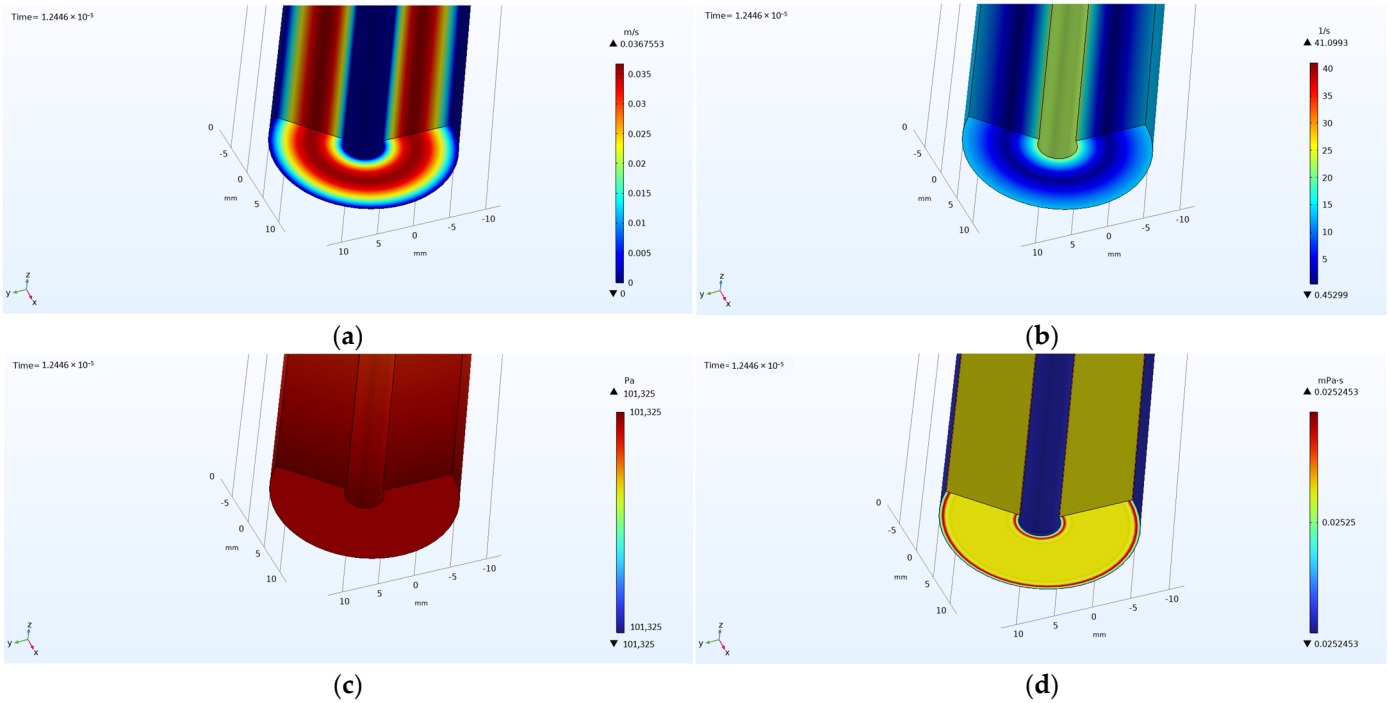

Figure 9. Fluid dynamic behavior for an experimental reactor at t = 12.446 µs as: (**a**) velocity (m/s), (**b**) vorticity (1/s), (**c**) pressure (Pa), and (**d**) dynamic viscosity (mPa·s).

4.2. Case Study Analysis

With the aim of improving plasma generation, thus optimizing conversion in the reactor, adapting several variables can be of interest.

In the earlier 1D-Geometry study, the influence of voltage and frequency were already examined, indicating that future experimental set-ups would benefit with higher voltage and maintaining, or slightly increasing, the system's frequency. Evidently, a trade-off between reactor conversion and energy efficiency exists; thus, only increasing voltage through sustainable means should be considered.

For this 2D-Geometry, the optimization of the reactor for future experiments can be obtained by studying the effects of the inlet volumetric rate, dielectric barrier thickness and material, and reactor length. All plasma properties presented below are average values at 12.446 µs when the plasma begins to stabilize.

4.2.1. Influence of Volumetric Inflow Rate

This case study analysis compares different gas flow cases with the previous example case (Case 1.5 in Table 1).

Firstly, the impact of the volumetric inflow rate introduced in the reactor's inlet can be studied purely with regards to fluid flow, as visualized in Figure 10. The graphs

compared the average velocity (m/s) and average pressure (Pa) across all cases with the total volumetric inflow rate between the following models: fluid flow, plasma study (without reactions), and plasma study (with reactions). The fluid flow and plasma study (without reactions) velocities indicate identical behavior. This allows the conclusion that the fluid interpretation of the plasma study is correct and aligned with prior contributions [48] of pure CFD results. Once the plasma reactions are introduced within the same geometry and conditions, the average velocity across the reactor reduces.

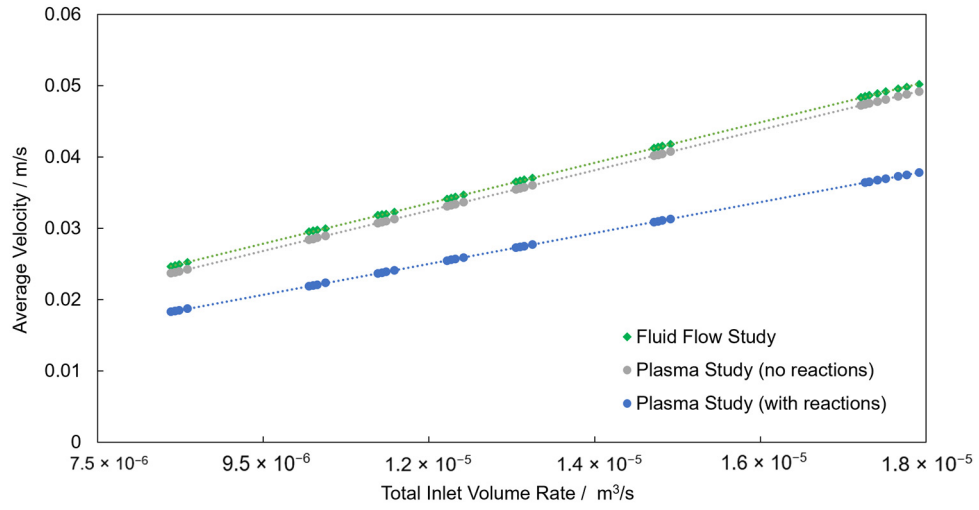

(**a**)

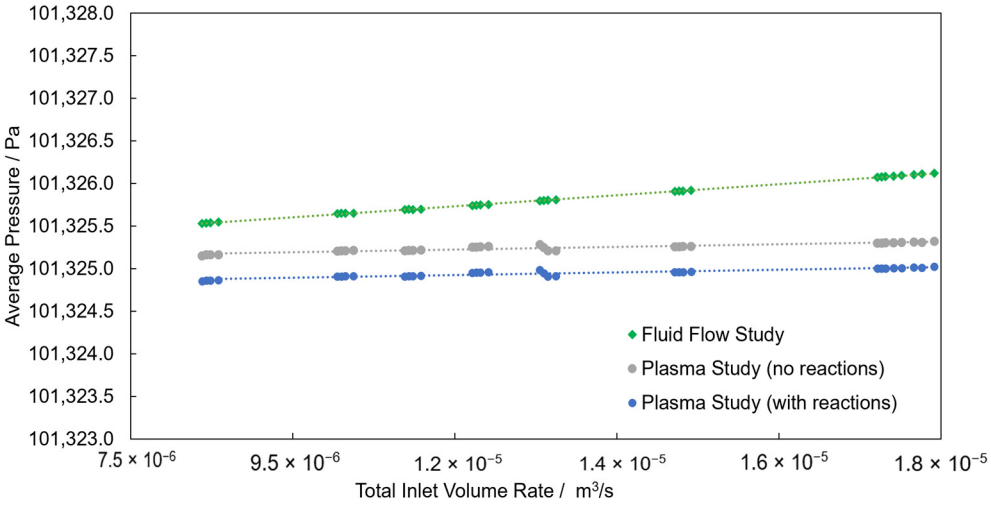

(**b**)

Figure 10. Comparison between the fluid flow study and plasma study (no reactions, with reactions) against total inlet volume rate for: (**a**) average velocity (m/s) and (**b**) average pressure (Pa).

Focusing on the velocity, for instance, the highest velocity both in the CFD studies and in this work are found in the vicinity of the inlet/outlet and around the geometry walls. Within the discharge gap itself, the velocity reduces in both studies, which is significant as the plasma is maintained in that location.

In the case of pressure, very little deviance is found between the models as the differences are almost negligible.

Secondly, noting the plasma behavior, the comparison between the experimental and plasma study on the effect of increasing inlet volume rate is presented in Figure 11, focusing on the electron density. Experimetal yield results studying the impact of inlet volumetric rate are found in Table 1 in earlier sections.

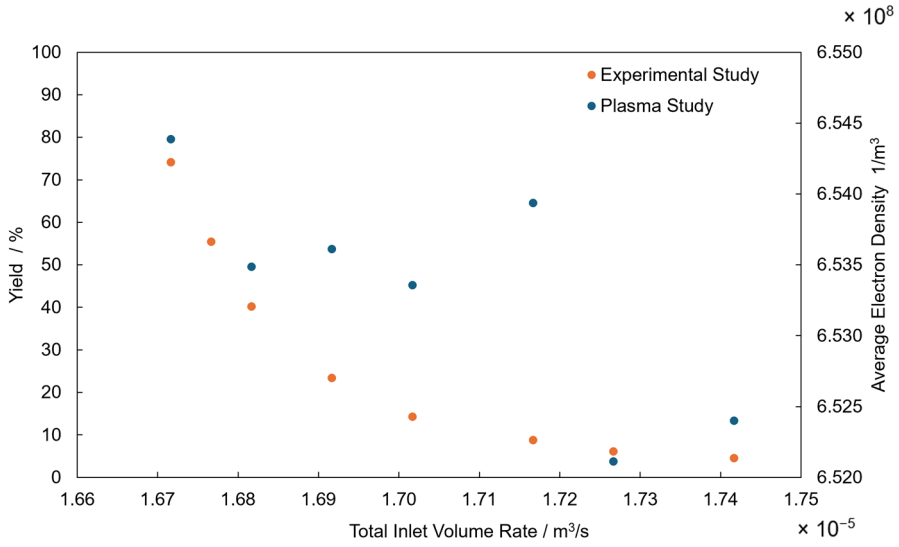

Figure 11. Comparison between the experimental study and plasma flow in electron density.

The behavior between the experimental yield and the electron density is comparable, since both variables show an increase in magnitude nearing the lowest total inlet volume rate. To note, similar behaviors are observed for excited argon and argon ion molar concentrations.

Yet, the discrepancies found can be attributed to a few points. Firstly, most notably, while experiments include the CO_2-Ar mixture, the simulations only consider argon. In fact, the highest yield (%) is obtained with the highest argon concentration. Secondly, the plasma study indicates electron density results at a given time iteration (12.446 µs) of the time-dependent study and as an average across (r, Z) coordinates, as a representative value, to simplify a high amount of data points. Finally, while experimental results allow the computation of conversion, this is not possible computationally, as the molar concentration of CO_2 is not obtainable; therefore, two different variables must be compared.

Although discrepancies appear, the focus must be on the collisions of all species in the reactor. It is expected that the higher the electron density in the reactor, the higher the probability of collisions occurring. These collisions can create radicals that provide enough energy to break the OC=O bond (at ~2.94 eV) and form new compounds. Thus, although CO_2 concentrations are not quantifiable with the simulation, an assumption can be made that the higher the electron density, the higher the probability of collisions to occur, and the more collisions occur, the higher the probability of CO to be generated.

4.2.2. Influence of Dielectric Barrier Material

The dielectric barrier material is not as easily adapted in an experimental set-up as in computations. Previous literature is available where the effect of dielectric constant and secondary electron emission coefficient on discharge characteristics is studied [66]. When considering the influence on the dielectric materials, results between authors differ, some considering that the conductivity of the dielectric can be a crucial factor in discharge properties as seen by Belov et al. [67], while Aerts et al. [26] reported no significant effect between alumina and quartz under wide-ranging conditions. Some authors, Li et al. [19,20] and Wang et al. [21], have focused their efforts on developing more sophisticated dielectric materials ($Ca_{0.8}Sr_{0.2}TiO_3$ (CST) with 0.5 wt% Li_2Si_2O as dielectric barrier), achieving an improvement in conversion by a factor of up to 9, compared to silica glass. While different dielectrics may allow for easier igniting and streamer formation, this does not necessarily translate to more energy-efficient plasma chemistry.

In the case of this work, a similar comparison between dielectric barriers for the given reactor can be simulated. As noted earlier, the relative permittivity of quartz can range from

3.9 to 10 [23]. In addition, if the material itself changes, the secondary electron emission coefficient and mean energy of secondary electrons also change.

The following computations compare different dielectric materials and their respective properties, as presented in Table 7. The results are visualized in Figure 12.

Table 7. Dielectric constant (ε_r), secondary emissions coefficients (γ_p), and mean energy of secondary electrons (ε_p) of dielectric barrier materials.

Material	ε_r	Ref.	γ_p	Ref.	ε_p	Ref.
SiO_2 (quartz)	3.9, 4.2	[55]	0.2	[64]	6.154	[65]
MgO (ceramic)	9.9	[68]	0.15	[64]	5.920	[69]
Al_2O_3 (corundum)	9	[70]	0.155	[64]	1.800	[71]

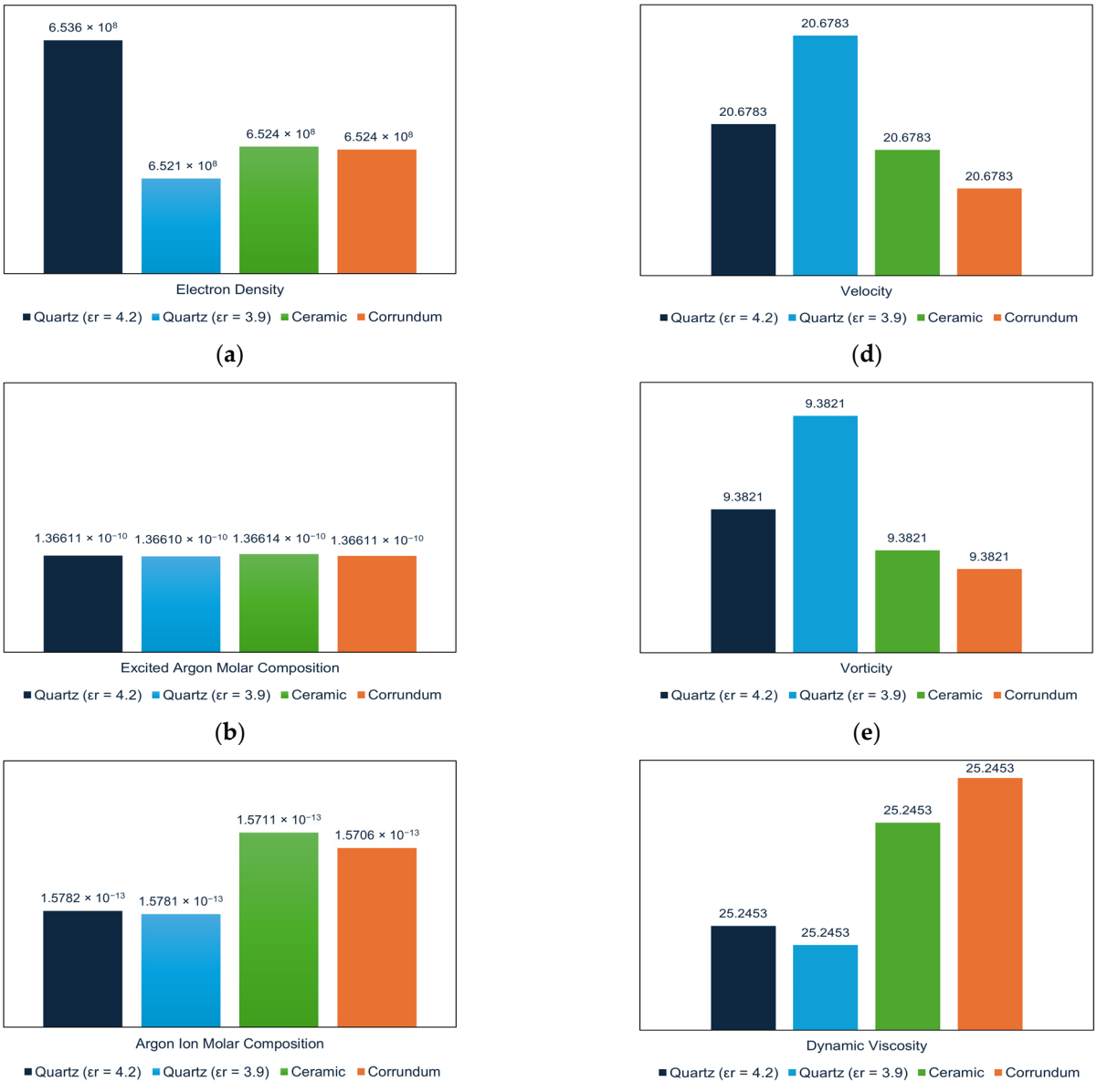

Figure 12. Effect of reactor dielectric material at 12.446 µs on: (**a**) electron density ($1/m^3$), (**b**) excited argon atoms molar concentration (mol/m^3), (**c**) argon ions molar concentration (mol/m^3), (**d**) velocity (mm/s), (**e**) vorticity (1/s), and (**f**) dynamic viscosity (µPa·s).

In these simulations, the effect of changing dielectric materials on plasma and fluid properties is noted. It is significant to point out that the comparison is performed at a specific time iteration, therefore the evolution of the plasma properties is not analyzed.

As expected, when comparing ε_r = 3.9–4.2 of quartz, the greater the relative permittivity, the greater the effect of the dielectric barrier and thus the higher the electron density. This effect is not as evident when comparing the molar composition of excited species and ions, but is still relevant, as slightly higher values are obtained. Although other materials (MgO, Al_2O_3) have even higher dielectric constants, their average electron density is not higher in comparison to quartz. This can be attributed to the different SEE coefficients and mean energy of secondary electrons. Nonetheless, both materials show a greater production of argon ions when compared to quartz.

The fluid properties in general show a very similar behavior for all studied cases with minimal changes. The velocity and vorticity behave in an analogous manner, while the dynamic viscosity mirrors them. A higher average velocity might be linked to lower electron density, but not necessarily to a higher molar concentration of argon ions.

This work concludes that changing the dielectric material can, in some cases, be advantageous. The results indicate that materials with a larger dielectric constant should be prioritized. However, the change in material must also consider the SEE coefficient and mean energy of secondary electrons in the wall.

4.2.3. Influence of Dielectric Thickness

In addition to the dielectric material, the dielectric thickness, which also affects the discharge gap, can also be studied. Other literature has shown effective DBD gaps of <10 mm [72]. For reference, in the case of Yu et al. [27], the author's contributions studied possible geometry modifications such as the discharge length and discharge gap. The authors found that changing the discharge gap appears to affect the discharge behavior and reactor conversion. Additional contributions [26] have shown that above a certain discharge gap width, less streamer formation occurs, which leads to less effective plasma volume and diminished conversions and efficiencies.

The experimental reactor is built with a quartz cylinder thickness of 0.5 mm, while other thicknesses simulated here are 1 mm, 1.5 mm, and 2 mm. The results of the effects of changing discharge thickness are provided in Figure 13.

Firstly, the comparison indicates that the excited argon molar composition decreases linearly with the increasing dielectric thickness. This is not necessarily the case with the argon ion molar composition, where a maximum is reached with 1 mm. Interestingly, the electron density acts in a mirrored manner, indicating its highest value with 2 mm. When performing the simulations, convergence of the model is more easily obtained with 1 mm and 2 mm thickness than other cases.

As expected, with increasing thickness, thus a smaller discharge gap, plasma ought to be formed with greater ease, and higher conversion should be achieved. These results suggest that increasing the dielectric thickness from 0.5 mm to 1 mm could provide beneficial results. In addition, other geometries, such as including another concentrical dielectric barrier, as presented in other contributions [41], could be advantageous.

When observing the fluid properties, the velocity, vorticity, and dynamic viscosity depend linearly on the reactor's gap. This is expected simply due to the volumetric changes of the plasma.

For the dielectric barrier thickness, a cylinder of 1 mm ought to be considered for future experiments since benefits in plasma steady state and argon ion production are observed.

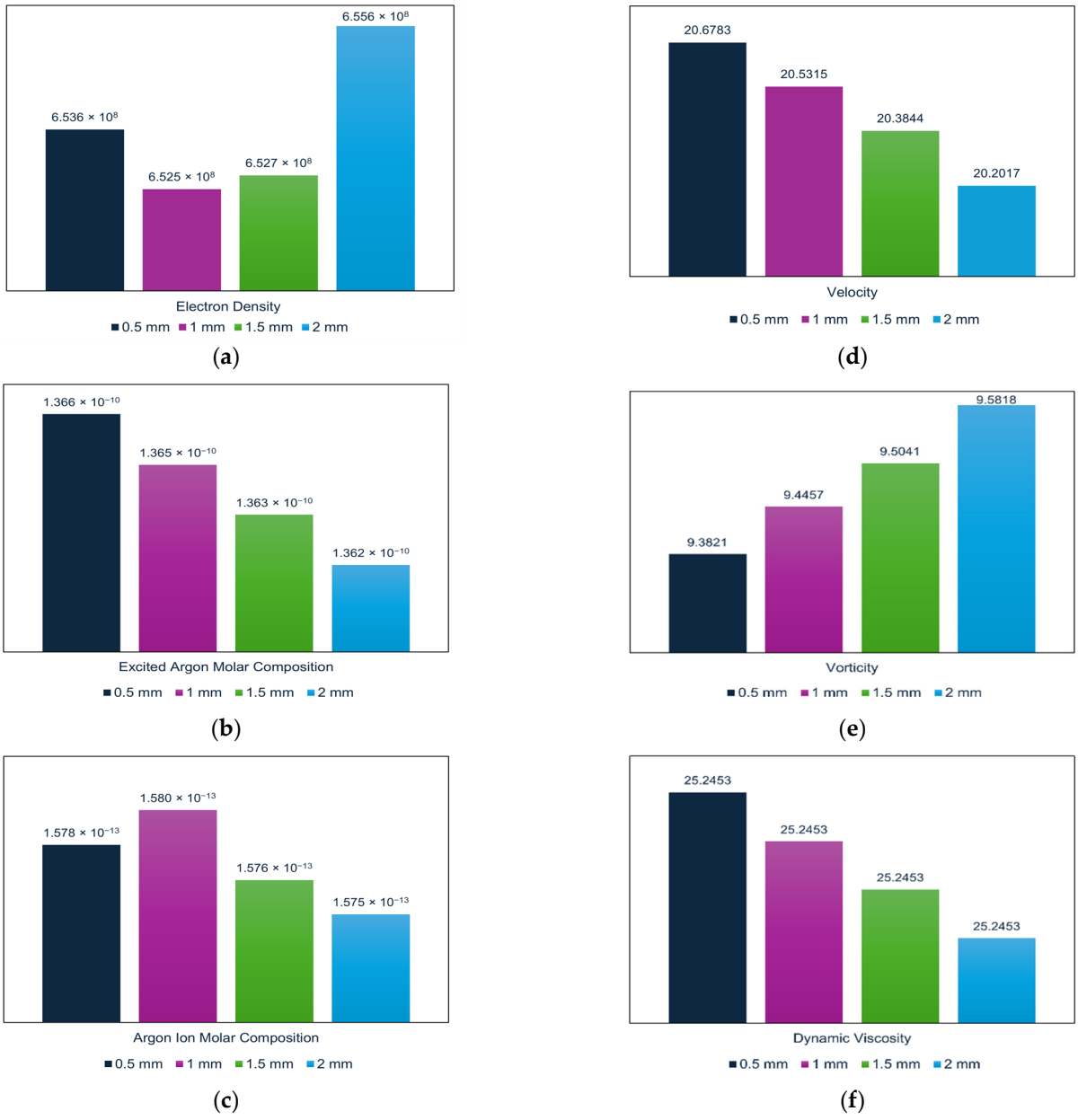

Figure 13. Effect of dielectric thickness at 12.446 µs on: (**a**) electron density ($1/m^3$), (**b**) excited argon atoms molar concentration (mol/m^3), (**c**) argon ions molar concentration (mol/m^3), (**d**) velocity (mm/s), (**e**) vorticity ($1/s$), and (**f**) dynamic viscosity ($\mu Pa{\cdot}s$).

4.2.4. Influence of Reactor Length

Further optimization of argon ionization can be studied with cases adapting the reactor length. Previous contributions, Yu et al. [27], have found that changing the discharge length for a fixed SEI in a specific reactor does not necessarily show any significant positive effects on plasma behavior. However, for this reactor, the impact is simulated below and represented in Figure 14.

In fact, a correlation between reactor length and studied variables is found. Both electron density and excited argon molar composition generally increase with increasing reactor length. The highest argon ion composition is found in L = 210 mm, while the highest electron density is seen in L = 160 mm.

From a fluid flow perspective, the velocity, vorticity, and dynamic viscosity decrease with increasing length analogously. This seems logical, as with a shorter length, the velocity (linear) and vorticity (rotational motion) should increase.

Future experiments could consider a reactor length $L > 160$ mm; however, considering material costs, other reactor optimizations might be prioritized.

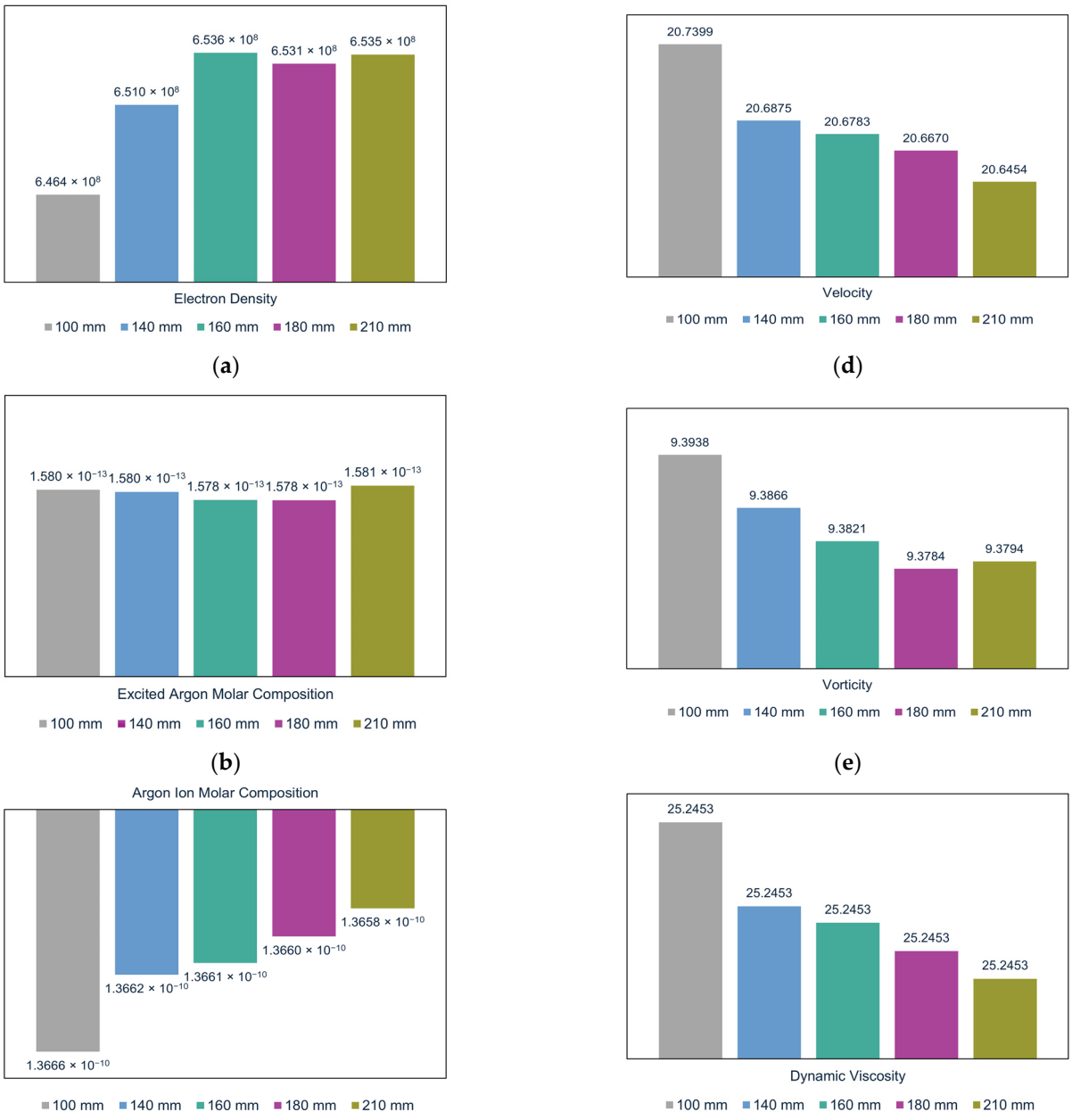

Figure 14. Effect of reactor length at 12.446 µs on: (**a**) electron density ($1/m^3$), (**b**) excited argon atoms molar concentration (mol/m^3), (**c**) argon ions molar concentration (mol/m^3), (**d**) velocity (mm/s), (**e**) vorticity (1/s), and (**f**) dynamic viscosity (µPa·s).

4.2.5. Fluid and Plasma Properties

Finally, the fluid and plasma properties are compared in the following section, as represented in Figure 15. In the graphs, the three plasma variables are represented against velocity and vorticity. The velocity and vorticity generally act in a mirrored manner. Although the graphs do not indicate fully symmetrical behavior, it can be generally concluded that an increasing velocity equates to a decreasing vorticity.

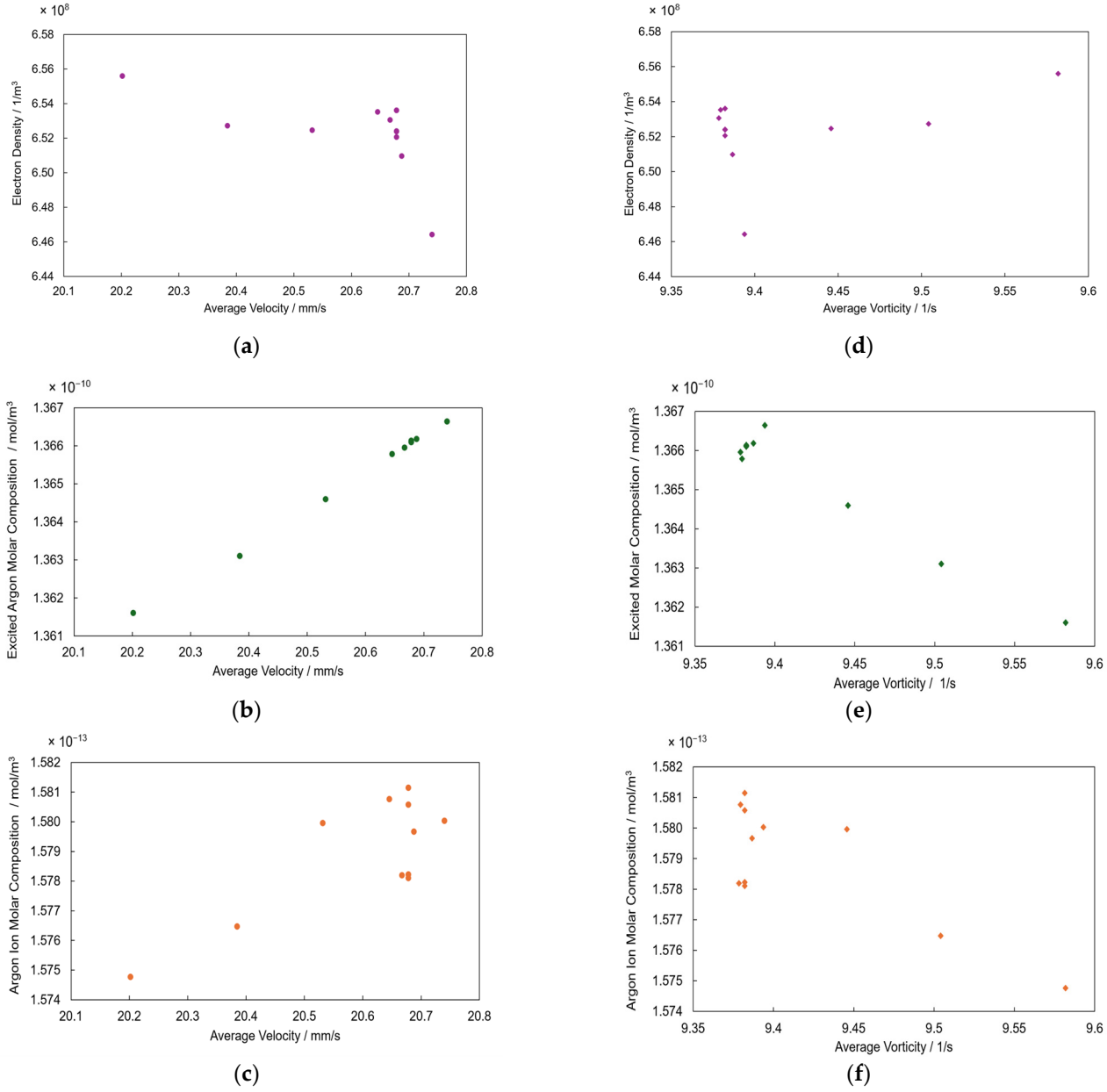

Figure 15. Comparison of fluid and plasma properties across study cases at 12.446 µs on: (**a**) electron density and velocity; (**b**) excited argon atoms molar concentration and velocity; (**c**) argon ions molar concentration and velocity; (**d**) electron density and vorticity; (**e**) excited argon atoms molar concentration and vorticity; and (**f**) argon ions molar concentration and vorticity.

The electron density shows an inverse correlation to the average velocity. In fact, the case with the lowest electron density showcases the greatest velocity in the reactor. The electron density can be a good metric to understand the effects of the introduction of electric potential; however, it is not necessarily the only metric to observe for optimum reactor conversion. The movement of electrons reach the wall very rapidly due to migration, as opposed to excited argon atoms, and also generate avalanches due to secondary emissions. Too high a velocity of the species in the plasma can jeopardize the effectiveness of the plasma, as the compounds may travel too quickly across the reactor.

Yet, when looking into the excited argon molar composition, the correlation found allows one to conclude that the higher the average velocity, the higher the concentration of excited argon species. However, the different cases only show a minor increase, which may be negligible. Such a direct correlation is also seen in the argon ions. The high

average velocity can indicate a large concentration of argon ions. Nonetheless, at highest velocities, the argon ion concentration stabilizes. Therefore, it is not possible to assume that a continuous increase in average velocity indicates an increasing amount of argon ions.

In broad terms, lower velocities and higher vorticity magnitudes in the given reactor can indicate plasma reactions and collisions to occur with higher probability. Nonetheless, too high a velocity of the species involved may not allow reactions to occur adequately, thus limiting the reactor's conversion.

5. Conclusions

In this work, the fluid study of a 2D-Geometry model simulating a non-thermal plasma with a dielectric barrier has been performed through a time-dependent study. The model has been built using pure argon, including thermodynamic characterization from previous contributions [49]. The plasma phenomena in the model are calculated for the relevant species, i.e., electrons, ground states, effective excited states, and ions. In addition, a computational fluid dynamics study is coupled to the plasma, with a laminar flow introduced in the inlet. To quicken computations, velocity and pressure values from previous CFD works [48] have been included as initial values in the model. The modeling results have also been compared to sets of experimental data [47] and computational fluid dynamics contributions [48].

With the initial reactor analysis, the plasma generation can be described with an example case at a given inlet volume rate. Plasma behavior is correctly described with the electron density, mass fraction of excited argon and argon ions, and mean electron energy. The model accounts for the excited/ionized species distribution across the reactor length, the electron density and movement, and the generation of the electric field near the anode. Additionally, the fluid flow is defined with the velocity, vorticity, pressure, and dynamic viscosity in the reactor.

In the case of the case study analysis, the impact of several variables on the plasma generation and fluid properties is evaluated.

- Firstly, the impact of volumetric inflow rate is noted from a pure fluid flow perspective as well as from a plasma perspective. The fluid flow is directly equivalent to the previous CFD contributions. Once the plasma reactions are introduced, the average velocity decreases in the reactor. The plasma behavior compares the experimental yield to the simulations, showing that yield can be linked to increasing electrons and excited species. Some discrepancies are noted due to the experiments including CO_2-Ar mixtures, while simulations are of pure argon.
- Secondly, the simulations indicate that changing the dielectric barrier material can be of interest. Generally, a higher dielectric constant is recommended; however, when introducing a new material, the effect of secondary emission coefficient and mean energy of secondary electrons must be included.
- Thirdly, apart from the dielectric material, changing the dielectric thickness can be beneficial. Smaller discharge gaps have shown significant benefits in simulation convergence. Future experiments could consider a dielectric thickness of 1 mm. In addition, including an additional concentric dielectric barrier, as in other works [41], could be of interest.
- Fourthly, the increased reactor length has shown an improvement in plasma generation, which could also be introduced. Future works could aim at studying the optimized length of the reactor prior to introducing a new experimental set-up.
- Finally, the fluid and plasma properties are compared to allow further understanding of the reactor behavior. A correlation between the electrons, excited species, and ions is found with the fluid behavior per case.

As previously stated, while the experiments were performed with carbon dioxide and a high concentration of argon gas (at least 95.69%), the simulation model is limited to studying pure argon. This is due to not only the fact that the chemical kinetic modeling

of the mixture in non-thermal conditions is not available, but also that considering all interactions of the mixtures in a 2D-Geometry would be computationally too demanding.

Nonetheless, to understand the conversion to CO, the focus must be on the collisions of all species in the reactor. In effect, the higher the electron density, excited argon atoms, and argon ions, the higher the probability of collisions occurring. These collisions create radicals that provide enough energy to break the OC=O bond and form new compounds; therefore, the more collisions occur, the higher probability of CO to be generated. As seen in the Mean Electron Energy section, the validity of the model can be confirmed as the dissociation energy required to break the CO=O bond (∼2.94 eV) is reached. Hence, although the CO obtained is not quantifiable with the simulation, the reactor's performance (probability of collisions occurring) can be linked to the concentration of electrons, ions, and excited atoms produced.

Upcoming experimental set-ups could introduce various optimizations, such as changing the inlet volumetric rate, introducing a dielectric material with higher relative permittivity, increasing the dielectric thickness, and/or adapting reactor length. Changing the cylindrical DBD piece would incur experimental costs and could require other reactor input variables to be further optimized. Increasing the reactor's length should improve the plasma efficiency but would also translate to laboratory expenses. Adapting the argon inlet flow rate to further increase CO_2 conversion could be a reasonable initial approach for future experiments.

Other simulation improvements could be aimed at including copper-based catalysts as porous media or geometry elements in the model, as well as introducing further reactants (and relevant reactions and collisions) significant in CO_2 conversion. However, these simulation enhancements would affect the computational burden of the tool; thus, other simplifications in the model could be required.

Author Contributions: Conceptualization, C.M.-P. and J.O.P.; methodology, C.M.-P.; investigation, C.M.-P., J.O.P. and F.L.; resources, J.O.P.; writing—original draft preparation, C.M.-P. and J.O.P.; writing—review and editing, C.M.-P., J.O.P. and F.L.; supervision, J.O.P. and F.L.; project administration, J.O.P. and F.L.; funding acquisition, J.O.P. and F.L. All authors have read and agreed to the published version of the manuscript.

Funding: This research was funded by La Caixa grant number (2018-LC-13) and AGAUR (2021 BP 0029).

Data Availability Statement: Data are contained within the article.

Acknowledgments: GESPA Group has been recognized as a Consolidated Research Group by the Catalan Government with code 2021-SGR-00321.

Conflicts of Interest: The authors declare that they have no known competing financial interests or personal relationships that could have appeared to influence the work reported in this paper.

References

1. Khan, T.M.; Khan, S.U.; Khan, S.U.; Ahmad, A.; Abbasi, S.A. A New Strategy of Using Dielectric Barrier Discharge Plasma in Tubular Geometry for Surface Coating and Extension to Biomedical Application. *Rev. Sci. Instrum.* **2020**, *91*, 073902. [CrossRef]
2. Chankuson, P.; Chumsri, P.; Plodkaew, A. The Simulation of Dielectric Barrier Discharge for Breakdown Voltage in Starch Modification. *Appl. Sci.* **2023**, *13*, 12143. [CrossRef]
3. Song, J.; Lv, J.; Pan, Y.; Wang, J.; Wang, J.; Cao, A.; Wu, A.; Williams, P.T.; Huang, Q. Low-Temperature Hydrogen Production from Waste Polyethylene by Nonthermal Plasma (NTP)-Assisted Catalytic Pyrolysis Using NiCeOx/β Catalyst. *Chem. Eng. J.* **2024**, *490*, 151676. [CrossRef]
4. Zhu, Q. Developments on CO_2-Utilization Technologies. *Clean Energy* **2019**, *3*, 85–100. [CrossRef]
5. Mei, D.; Tu, X. Conversion of CO_2 in a Cylindrical Dielectric Barrier Discharge Reactor: Effects of Plasma Processing Parameters and Reactor Design. *J. CO_2 Util.* **2017**, *19*, 68–78. [CrossRef]
6. Amouroux, J.; Cavadias, S.; Doubla, A. Carbon Dioxide Reduction by Non-Equilibrium Electrocatalysis Plasma Reactor. *IOP Conf. Ser. Mater. Sci. Eng.* **2011**, *19*, 12005. [CrossRef]
7. Ashford, B.; Tu, X. Non-Thermal Plasma Technology for the Conversion of CO_2. *Curr. Opin. Green Sustain. Chem.* **2017**, *3*, 45–49. [CrossRef]
8. Pou, J.O.; Colominas, C.; Gonzalez-Olmos, R. CO_2 Reduction Using Non-Thermal Plasma Generated with Photovoltaic Energy in a Fluidized Reactor. *J. CO_2 Util.* **2018**, *27*, 528–535. [CrossRef]

9. Saeidi, S.; Amin, N.A.S.; Rahimpour, M.R. Hydrogenation of CO_2 to Value-Added Products—A Review and Potential Future Developments. *J. CO_2 Util.* **2014**, *5*, 66–81. [CrossRef]
10. Khan, A.A.; Tahir, M. Recent Advancements in Engineering Approach towards Design of Photo-Reactors for Selective Photocatalytic CO_2 Reduction to Renewable Fuels. *J. CO_2 Util.* **2019**, *29*, 205–239. [CrossRef]
11. Kumar, B.; Llorente, M.; Froehlich, J.; Dang, T.; Sathrum, A.; Kubiak, C.P. Photochemical and Photoelectrochemical Reduction of CO_2. *Annu. Rev. Phys. Chem.* **2012**, *63*, 541–569. [CrossRef]
12. Yaashikaa, P.R.; Senthil Kumar, P.; Varjani, S.J.; Saravanan, A. A Review on Photochemical, Biochemical and Electrochemical Transformation of CO_2 into Value-Added Products. *J. CO_2 Util.* **2019**, *33*, 131–147. [CrossRef]
13. Cuéllar-Franca, R.M.; Azapagic, A. Carbon Capture, Storage and Utilisation Technologies: A Critical Analysis and Comparison of Their Life Cycle Environmental Impacts. *J. CO_2 Util.* **2015**, *9*, 82–102. [CrossRef]
14. Lindon, M.A.; Scime, E.E. CO_2 Dissociation Using the Versatile Atmospheric Dielectric Barrier Discharge Experiment (VADER). *Front. Phys.* **2014**, *2*, 55. [CrossRef]
15. Snoeckx, R.; Bogaerts, A. Plasma Technology—A Novel Solution for CO_2 Conversion? *Chem. Soc. Rev.* **2017**, *46*, 5805–5863. [CrossRef] [PubMed]
16. Zhang, T.; Lu, N.; Shang, K.; Jiang, N.; Li, J.; Wu, Y. Conversion of CO_2 in a Gliding Arc Discharge Reactor: Discharge Characteristics and the Effects of Different Parameters. *J. Phys. Conf. Ser.* **2021**, *2076*, 012103. [CrossRef]
17. Michielsen, I.; Uytdenhouwen, Y.; Pype, J.; Michielsen, B.; Mertens, J.; Reniers, F.; Meynen, V.; Bogaerts, A. CO_2 Dissociation in a Packed Bed DBD Reactor: First Steps towards a Better Understanding of Plasma Catalysis. *Chem. Eng. J.* **2017**, *326*, 477–488. [CrossRef]
18. Zhu, H.; Huang, Y.; Yin, S.; Zhang, W. Microwave Plasma Setups for CO_2 Conversion: A Mini-Review. *Green Energy Resour.* **2024**, *2*, 100061. [CrossRef]
19. Li, R.; Tang, Q.; Yin, S.; Sato, T. Plasma Catalysis for CO_2 Decomposition by Using Different Dielectric Materials. *Fuel Process. Technol.* **2006**, *87*, 617–622. [CrossRef]
20. Li, R.; Tang, Q.; Yin, S.; Sato, T. Investigation of Dielectric Barrier Discharge Dependence on Permittivity of Barrier Materials. *Appl. Phys. Lett.* **2007**, *90*, 131502. [CrossRef]
21. Wang, S.; Zhang, Y.; Liu, X.; Wang, X. Enhancement of CO_2 Conversion Rate and Conversion Efficiency by Homogeneous Discharges. *Plasma Chem. Plasma Process.* **2012**, *32*, 979–989. [CrossRef]
22. Fridman, A.; Chirokov, A.; Gutsol, A. Non-Thermal Atmospheric Pressure Discharges. *J. Phys. D Appl. Phys.* **2005**, *38*, R1–R24. [CrossRef]
23. Kogelschatz, U. Dielectric-Barrier Discharges: Their History, Discharge Physics, and Industrial Applications. *Plasma Chem. Plasma Process.* **2003**, *23*, 1–46. [CrossRef]
24. Ramakers, M.; Michielsen, I.; Aerts, R.; Meynen, V.; Bogaerts, A. Effect of Argon or Helium on the CO_2 Conversion in a Dielectric Barrier Discharge. *Plasma Process. Polym.* **2015**, *12*, 755–763. [CrossRef]
25. Ozkan, A.; Dufour, T.; Silva, T.; Britun, N.; Snyders, R.; Bogaerts, A.; Reniers, F. The Influence of Power and Frequency on the Filamentary Behavior of a Flowing DBD—Application to the Splitting of CO_2. *Plasma Sources Sci. Technol.* **2016**, *25*, 025013. [CrossRef]
26. Aerts, R.; Somers, W.; Bogaerts, A. Carbon Dioxide Splitting in a Dielectric Barrier Discharge Plasma: A Combined Experimental and Computational Study. *ChemSusChem* **2015**, *8*, 702–716. [CrossRef] [PubMed]
27. Yu, Q.; Kong, M.; Liu, T.; Fei, J.; Zheng, X. Characteristics of the Decomposition of CO_2 in a Dielectric Packed-Bed Plasma Reactor. *Plasma Chem. Plasma Process.* **2012**, *32*, 153–163. [CrossRef]
28. Paulussen, S.; Verheyde, B.; Tu, X.; De Bie, C.; Martens, T.; Petrovic, D.; Bogaerts, A.; Sels, B. Conversion of Carbon Dioxide to Value-Added Chemicals in Atmospheric Pressure Dielectric Barrier Discharges. *Plasma Sources Sci. Technol.* **2010**, *19*, 034015. [CrossRef]
29. Wang, J.-Y.; Xia, G.-G.; Huang, A.; Suib, S.L.; Hayashi, Y.; Matsumoto, H. CO_2 Decomposition Using Glow Discharge Plasmas. *J. Catal.* **1999**, *185*, 152–159. [CrossRef]
30. Mei, D.; Zhu, X.; He, Y.; Yan, J.D.; Tu, X. Plasma-Assisted Conversion of CO_2 in a Dielectric Barrier Discharge Reactor: Understanding the Effect of Packing Materials. *Plasma Sources Sci. Technol.* **2014**, *24*, 015011. [CrossRef]
31. Bogaerts, A.; Snoeckx, R.; Trenchev, G.; Wang, W. Modeling for a Better Understanding of Plasma-Based CO_2 Conversion. In *Plasma Chemistry and Gas Conversion*; Intechopen: London, UK, 2018.
32. MacHrafi, H.; Cavadias, S.; Amouroux, J. CO_2 Valorization by Means of Dielectric Barrier Discharge. *J. Phys. Conf. Ser.* **2011**, *275*, 012016. [CrossRef]
33. Ponduri, S.; Becker, M.M.; Welzel, S.; van de Sanden, M.C.M.; Loffhagen, D.; Engeln, R. Fluid Modelling of CO_2 Dissociation in a Dielectric Barrier Discharge. *J. Appl. Phys.* **2016**, *119*, 093301. [CrossRef]
34. Trenchev, G.; Bogaerts, A. Dual-Vortex Plasmatron: A Novel Plasma Source for CO_2 conversion. *J. CO_2 Util.* **2020**, *39*, 101152. [CrossRef]
35. Barkaoui, G.; Halima, A.B.; Jomaa, N.; Charrada, K.; Yousfi, M. A Numerical Simulation of a Low-Temperature Argon Plasma Jet. *IEEE Trans. Plasma Sci.* **2021**, *49*, 1302–1310. [CrossRef]
36. Sharma, N.K.; Misra, S.; Varun; Pal, U.N. Experimental and Simulation Analysis of Dielectric Barrier Discharge Based Pulsed Cold Atmospheric Pressure Plasma Jet. *Phys. Plasmas* **2020**, *27*, 113502. [CrossRef]

37. Schweigert, I.; Zakrevsky, D.; Gugin, P.; Yelak, E.; Golubitskaya, E.; Troitskaya, O.; Koval, O. Interaction of Cold Atmospheric Argon and Helium Plasma Jets with Bio-Target with Grounded Substrate Beneath. *Appl. Sci.* **2019**, *9*, 4528. [CrossRef]
38. Khan, T.M.; Khan, S.U.-D.; Raffi, M.; Khan, R. Theoretical–Computational Study of Atmospheric DBD Plasma and Its Utility for Nanoscale Biocompatible Plasmonic Coating. *Molecules* **2021**, *26*, 5106. [CrossRef]
39. Deepak, G.D.; Joshi, N.K.; Prakash, R. Modal Analysis of Dielectric Barrier Discharge-Based Argon Cold Plasma Jet. *Laser Part. Beams* **2020**, *38*, 229–238. [CrossRef]
40. Mehrabifard, R. Two-Dimensional Simulation of Argon Dielectric Barrier Discharge (DBD) in Plasma Actuator Structure with COMSOL Multiphysics Two-Dimensional Simulation of Argon Dielectric Barrier Discharge (DBD) Plasma Actuator with COMSOL Multiphysics. *Radiat. Phys. Eng.* **2023**, *4*, 43–50. [CrossRef]
41. Hosseinpour, M.; Zendehnam, A. Study of an Argon Dielectric Barrier Discharge Reactor with Atmospheric Pressure for Material Treatment. *J. Theor. Appl. Phys.* **2018**, *12*, 271–291. [CrossRef]
42. Stankov, M.; Becker, M.M.; Hoder, T.; Loffhagen, D. Extended Reaction Kinetics Model for Non-Thermal Argon Plasmas and Its Test against Experimental Data. *Plasma Sources Sci. Technol.* **2022**, *31*, 125002. [CrossRef]
43. Al-Khafaji, T.K. Effects of Variable Applied Voltage on Dielectric Barrier Discharge Plasma Parameters: Comparative Study. *Iraqi J. Appl. Phys.* **2024**, *20*, 405–410.
44. Jovanović, A.P.; Loffhagen, D.; Becker, M.M. Streamer-Surface Interaction in an Atmospheric Pressure Dielectric Barrier Discharge in Argon. *Plasma Sources Sci. Technol.* **2022**, *31*, 04LT02. [CrossRef]
45. Van Laer, K.; Bogaerts, A. Fluid Modelling of a Packed Bed Dielectric Barrier Discharge Plasma Reactor. *Plasma Sources Sci. Technol.* **2015**, *25*, 015002. [CrossRef]
46. Jovanović, A.P.; Hoder, T.; Höft, H.; Loffhagen, D.; Becker, M.M. Formation Mechanisms of Striations in a Filamentary Dielectric Barrier Discharge in Atmospheric Pressure Argon. *Plasma Sources Sci. Technol.* **2023**, *32*, 055011. [CrossRef]
47. Pou, J.O.; Estopañán, E.; Fernandez-Garcia, J.; Gonzalez-Olmos, R. Sustainability Assessment of the Utilization of CO_2 in a Dielectric Barrier Discharge Reactor Powered by Photovoltaic Energy. *Processes* **2022**, *10*, 1851. [CrossRef]
48. Mas-Peiro, C.; Llovell Ferret, F.; Pou Ibar, O. Computational Fluid Dynamic Study of Gas Mixtures in a Non-Thermal Plasma Reactor for CO_2 Conversion with Argon as Diluent Gas. *Afinidad. J. Chem. Eng. Theor. Appl. Chem.* **2024**, *81*, 58–68. [CrossRef] [PubMed]
49. Mas-Peiro, C.; Quinteros-Lama, H.; Pou, J.O.; Llovell, F. Thermodynamic Characterization of Gas Mixtures for Non-Thermal Plasma CO_2 Conversion Applications with Soft-SAFT. *J. Chem. Eng. Data* **2023**, *68*, 1376–1387. [CrossRef]
50. Thomas, G.; Beuthe, T.G.B.; Jen-Shih Chang, J.-S.C. Chemical Kinetic Modelling of Non-Equilibrium Ar-CO_2 Thermal Plasmas. *Jpn. J. Appl. Phys.* **1997**, *36*, 4997. [CrossRef]
51. Alkhatib, I.I.I.; Pereira, L.M.C.; Torne, J.; Vega, L.F. Polar Soft-SAFT: Theory and Comparison with Molecular Simulations and Experimental Data of Pure Polar Fluids. *Phys. Chem. Chem. Phys.* **2020**, *22*, 13171–13191. [CrossRef]
52. Llovell, F.; Vega, L.F. Prediction of Thermodynamic Derivative Properties of Pure Fluids through the Soft-SAFT Equation of State. *J. Phys. Chem. B* **2006**, *110*, 11427–11437. [CrossRef]
53. Chapman, W.G.; Gubbins, K.E.; Jackson, G.; Radosz, M. SAFT: Equation-of-State Solution Model for Associating Fluids. *Fluid Phase Equilibria* **1989**, *52*, 31–38. [CrossRef]
54. Johnson, J.K.; Zollweg, J.A.; Gubbins, K.E. The Lennard-Jones Equation of State Revisited. *Mol. Phys.* **1993**, *78*, 591–618. [CrossRef]
55. Bottom, V.E. Dielectric Constants of Quartz. *J. Appl. Phys.* **1972**, *43*, 1493–1495. [CrossRef]
56. Shahbazi Rad, Z.; Abbasi Davani, F. Non-Thermal Atmospheric Pressure Dielectric Barrier Discharge Plasma Source Construction and Investigation on the Effect of Grid on Wound Healing Application. *Clin. Plasma Med.* **2016**, *4*, 56–64. [CrossRef]
57. Mas-Peiro, C.; Llovell Ferret, F.; Pou Ibar, O. Simulation of a Non-Thermal Plasma Reactor with Dielectric Barrier Discharge for CO_2 Conversion. In Proceedings of the COMSOL Conference Munich, Munich, Germany, 25–27 October 2023.
58. COMSOL Multiphysics. *Plasma Module User's Guide*; Version 5.3; COMSOL, Inc.: Burlington, MA, USA, 2018.
59. COMSOL Multiphysics. *CFD Module User's Guide*; Version 5.4; COMSOL, Inc.: Burlington, MA, USA, 2018.
60. Phelps Database: LXCat. Available online: https://us.lxcat.net/ (accessed on 26 January 2024).
61. Hagelaar, G.J.M.; Pitchford, L.C. Solving the Boltzmann Equation to Obtain Electron Transport Coefficients and Rate Coefficients for Fluid Models. *Plasma Sources Sci. Technol.* **2005**, *14*, 722–733. [CrossRef]
62. Daksha, M.; Derzsi, A.; Mujahid, Z.; Schulenberg, D.; Berger, B.; Donkó, Z.; Schulze, J. Material Dependent Modeling of Secondary Electron Emission Coefficients and Its Effects on PIC/MCC Simulation Results of Capacitive RF Plasmas. *Plasma Sources Sci. Technol.* **2019**, *28*, 034002. [CrossRef]
63. Mitchell, E.W.J.; Mitchell, J.W. The Work Functions of Copper, Silver and Aluminium. *Proc. R. Soc. Lond. Ser. A Math. Phys. Sci.* **1951**, *210*, 70–84. [CrossRef]
64. Marbach, J.; Bronold, F.X.; Fehske, H. Resonant Charge Transfer at Dielectric Surfaces. *Eur. Phys. J. D* **2012**, *66*, 106. [CrossRef]
65. Mohanta, S.K.; Rath, S.S.; Dwari, R.K. Surface Functionalization of Coal and Quartz with Aniline: A Study on Work Function and Frictional Charge. *Powder Technol.* **2018**, *338*, 233–242. [CrossRef]
66. Zhao, N.; Yang, H.; Yao, C.; Wang, C.; Chen, C.; Dang, J.; Yang, X.; Chang, Z. Effects of Dielectric Constant and Secondary Electron Emission Coefficient on Discharge Characteristics and Products of Ar/NH3 DBD. *Phys. Plasmas* **2022**, *29*, 033512. [CrossRef]
67. Belov, I.; Paulussen, S.; Bogaerts, A. Appearance of a Conductive Carbonaceous Coating in a CO_2 Dielectric Barrier Discharge and Its Influence on the Electrical Properties and the Conversion Efficiency. *Plasma Sources Sci. Technol.* **2016**, *25*, 015023. [CrossRef]

68. Subramanian, M.A.; Shannon, R.D.; Chai, B.H.T.; Abraham, M.M.; Wintersgill, M.C. Dielectric Constants of BeO, MgO, and CaO Using the Two-Terminal Method. *Phys. Chem. Min.* **1989**, *16*, 741–746. [CrossRef]
69. Choi, E.H.; Lim, J.Y.; Kang, S.O.; Uhm, H.S. Measurement of Work Function at MgO Crystal Surface by the γ-Focused Ion Beam System. *Jpn. J. Appl. Phys.* **2002**, *41*, L1006–L1009. [CrossRef]
70. McPherson, J.W.; Kim, J.; Shanware, A.; Mogul, H.; Rodriguez, J. Trends in the Ultimate Breakdown Strength of High Dielectric-Constant Materials. *IEEE Trans. Electron. Devices* **2003**, *50*, 1771–1778. [CrossRef]
71. Liu, M.; Jin, Y.; Chen, B.; Leygraf, C.; Wang, L.; Pan, J. Density Functional Theory Study of Influence of Oxide Thickness and Surface Alloying on Cl Migration within α-Al_2O_3. *J. Electrochem. Soc.* **2021**, *168*, 081508. [CrossRef]
72. Brandenburg, R. Corrigendum: Dielectric Barrier Discharges: Progress on Plasma Sources and on the Understanding of Regimes and Single Filaments. *Plasma Sources Sci. Technol.* **2017**, *26*, 053001. [CrossRef]